

# On the Benefits of Instance Decomposition in Video Prediction Models

Eliyas Suleyman<sup>1</sup>, Paul Henderson<sup>1</sup>, Nicolas Pugeault<sup>1</sup>

<sup>1</sup>School of Computing Science, University of Glasgow  
2683522s@student.gla.ac.uk, {paul.henderson,nicolas.pugeault}@glasgow.ac.uk

## Abstract

Video prediction is a crucial task for intelligent agents such as robots and autonomous vehicles, since it enables them to anticipate and act early on time-critical incidents. State-of-the-art video prediction methods typically model the dynamics of a scene jointly and implicitly, without any explicit decomposition into separate objects. This is challenging and potentially sub-optimal, as every object in a dynamic scene has their own pattern of movement, typically somewhat independent of others. In this paper, we investigate the benefit of explicitly modeling the objects in a dynamic scene separately within the context of latent-transformer video prediction models. We conduct detailed and carefully-controlled experiments on both synthetic and real-world datasets; our results show that decomposing a dynamic scene leads to higher quality predictions compared with models of a similar capacity that lack such decomposition.

## 1 Introduction

Video prediction is the task of predicting future frames based on past frames; it has many applications including autonomous driving (Yang et al. 2024), weather forecasting from satellite images (Ravuri et al. 2021), and even building general world models (Wang et al. 2024). Predicting future frames is challenging, since these are high-dimensional and result from multiple objects’ appearances, dynamics and mutual interactions. For example, consider the environment observed while driving a car. To accurately predict the future, we must identify all objects in our field of vision and estimate their likely movements. Different types of objects (e.g. cars, pedestrians, dogs) have very different appearances, but also diverse patterns of movement, and may exhibit complex interactions with other objects.

To reduce this complexity, a natural approach to video prediction is to decompose the scene into several parts (Sun et al. 2023; Bei, Yang, and Soatto 2021; Lee et al. 2021; Hsieh et al. 2018). This enables modeling the appearance and dynamics of each part separately during prediction, thus reducing computational cost and increasing statistical efficiency. Several works have achieved promising results by such approaches, using different choices of decomposition. For example, (Hsieh et al. 2018) uses DRNet (Denton et al. 2017) to learn a disentangled representation of appearance and 2D pose, while (Bei, Yang, and Soatto 2021; Lee et al.

2021) use semantic segmentation models, and (Sun et al. 2023) separates the foreground, motion and background. (Wu et al. 2022) uses object-centric representation learning (Locatello et al. 2020) to separate objects without supervision, and model the dynamics with a multi-slot transformer.

While these works on object-decomposed prediction often achieve impressive results, they do not typically focus on measuring the benefit of object decomposition in a scientifically-controlled way, i.e. keeping confounding factors such as the number of network parameters, architecture or latent dimensionality constant. Moreover, most of these works did not use the modern large latent-space Transformer architectures (Vaswani et al. 2017) that now yield excellent results on diverse domains of videos (Yan et al. 2021; Wu et al. 2024); they instead used older, smaller CNN- or RNN-based models.

In this work, we perform a detailed study of the benefits of explicitly modeling different objects separately during video prediction, when using modern latent transformer models. Rather than introducing an entirely new model, we develop a family of architectures that uses ideas from VideoGPT, MOSO and Slotformer (Yan et al. 2021; Sun et al. 2023; Wu et al. 2022), but supports both monolithic and object-decomposed prediction in a unified framework. This allows us to perform controlled experiments on the benefits of object decomposition and strategies for modeling interactions. Specifically, we adopt a hierarchical approach that explicitly decomposes a dynamic scene into individual objects using an instance segmentation model, before encoding these into separate latent spaces. Going beyond previous approaches, we also mitigate the inefficiency of having separate network parameters per object instance (Villar-Corrales, Wahdan, and Behnke 2023) by sharing parameters across all instances of each class.

We find that even with large transformers, object decomposition leads to considerable improvements in handling complex scenes with multiple interacting objects compared to non-object-centric predictors with similar parameter counts and latent dimensions.

Our main contributions are as follows:

- We present the first systematic and comprehensive analysis of the benefits of explicit object decomposition for latent transformer video prediction models.
- To achieve this, we develop a scalable framework for

video prediction that supports both the object-centric and nondecomposed settings.

- We mitigate inefficiencies in object-centric video predictors by sharing weights (and thus knowledge about object dynamics) across slots within each object class.

## 2 Related Work

**Recurrent models for video prediction** Early video prediction models were typically based on the combination of Convolutional Neural Networks (Krizhevsky, Sutskever, and Hinton 2012) and Recurrent Neural Networks, often LSTMs (Shi et al. 2015; Wang et al. 2022, 2018; Chang et al. 2022; Gao et al. 2022; Denton and Fergus 2018). (Lee et al. 2021) proposed a method to predict future semantic maps, then used those predicted maps to formulate the actual future frames. (Bei, Yang, and Soatto 2021) proposed a similar approach which decomposes the scene by semantic map then use separate pathways to model the dynamics of different semantic classes. Of these, some methods are deterministic, i.e. make a single most-likely prediction of the future (Shi et al. 2015; Wang et al. 2018), while others are stochastic, i.e. sample an autoregressive posterior distribution on possible future frames (Denton and Fergus 2018; Lee et al. 2021). We focus on the stochastic setting in this work since it reflects the fact that the future is inherently uncertain, as well as typically producing sharper predictions.

**Transformer models for video prediction** Following their success on text (Vaswani et al. 2017) and images (Dosovitskiy et al. 2020), Transformers have also been applied to video prediction. A common approach is to first use an encoder network to map the original video frames into a sequence of lower-dimensional latent vectors. Most models use VQ-VAE (van den Oord, Vinyals, and Kavukcuoglu 2017) or VQ-GAN (Esser, Rombach, and Ommer 2021) as their encoding network due to their high fidelity reconstruction of original frames, and discrete latent space that enables treating the latents similarly to text tokens. (Yan et al. 2021) proposed the first autoregressive video prediction model based on VQ-GAN and a decoder transformer to predict future frames; iVideoGPT (Wu et al. 2024) improves performance further. (Gupta et al. 2022) proposed a similar method that uses VQ-VAE and transformer, but trains with iterative masking to let it gradually capture the motion patterns in a video. (Sun et al. 2023) proposed a pipeline that decomposes the dynamic scene into motion, object and background, then uses a stochastic transformer to predict future frames in latent space. Our work also uses a latent transformer, but with an explicit decomposition of the latent space into separate objects, and cross-attention to capture object interactions.

**Diffusion models for video prediction** The invention of diffusion models (Sohl-Dickstein et al. 2015; Ho, Jain, and Abbeel 2020) and the computationally faster latent diffusion (Rombach et al. 2022) brought significant improvement on many generative tasks. Latent diffusion was originally designed to generate high-resolution images, but has now been applied to video (Blattmann et al. 2023b,a; Brooks et al.

2024). (Ho et al. 2022) use a diffusion model to generate long videos via a joint training paradigm with conditional sampling. (Höppe et al. 2022) use a slightly different training process that instead of adding noise to the entire video, randomly kept some of the input frames without noise. (Yu et al. 2023) proposed an interesting way of modelling latent vectors in three different direction by slicing 3D feature vectors along different axes. SORA (Brooks et al. 2024) is the state-of-the-art video generation model which can generate extremely realistic videos by using diffusion with a transformer architecture. It is able to accurately model complex interactions involving multiple objects (Liu et al. 2024).

**Object-centric video prediction** Object-centric representation learning aims to learn decomposed representations of images (Locatello et al. 2020; Engelcke et al. 2019) or videos (Jiang et al. 2019; Zhou et al. 2022) without supervision. This can be used to aid video prediction by learning an object-centric predictor (typically a transformer) over the resulting representations (Kipf et al. 2021; Li et al. 2021; Sajjadi et al. 2022; Singh, Wu, and Ahn 2022). (Villar-Corrales, Wahdan, and Behnke 2023) use an attention mechanism to learn the relationship between different objects in the video sequence and achieved good results on synthetic CLEVRER (Yi et al. 2019) dataset. (Schmeckpeper, Georgakis, and Daniilidis 2021) use Mask R-CNN (He et al. 2017) to get bounding boxes for each entity in the scene, then predict the next state of each bounding box from a single frame. Finally, (Henderson and Lampert 2020; Henderson, Lampert, and Bickel 2021) proposed self-supervised object-centric approaches that predict frames via latent 3D objects and scene structure from 2D video.

**Cross-attention** Our model uses cross-attention between instances to capture object interactions. Similar ideas have been used in many other domains, e.g. (Zhu et al. 2022) use pairwise cross-attention to re-identify pedestrians; (Shi et al. 2024) use cross-attention to fuse information from audio and video for emotion recognition; (Lee, Lee, and Choi 2023) use pairwise cross attention on video action recognition; (Rombach et al. 2022) uses cross attention between image features and text embeddings for conditional image generation.

## 3 Methodology

Let  $X^{1:T} = \langle x^1, x^2, \dots, x^T \rangle$ , be a sequence of  $T$  RGB frames from a video clip, where  $x^t \in \mathbb{R}^{h \times w \times 3}$ . Our goal is to learn a probability distribution on future frames  $X^{T+1:T+M}$ , conditioned on the preceding frames  $X^{1:T}$ .

We hypothesize that predicting future frames is more effective when modeling each object or instance separately rather than modeling the entire scene at once. Moreover, when objects are decomposed, we aim to measure the degree to which cross-attention enables learning interactions among objects, thus making prediction more accurate.

To test this hypothesis, we design a family of models that support differing degrees of object decomposition and interaction within a unified framework. We decompose a scene into individual objects using instance segmentation models

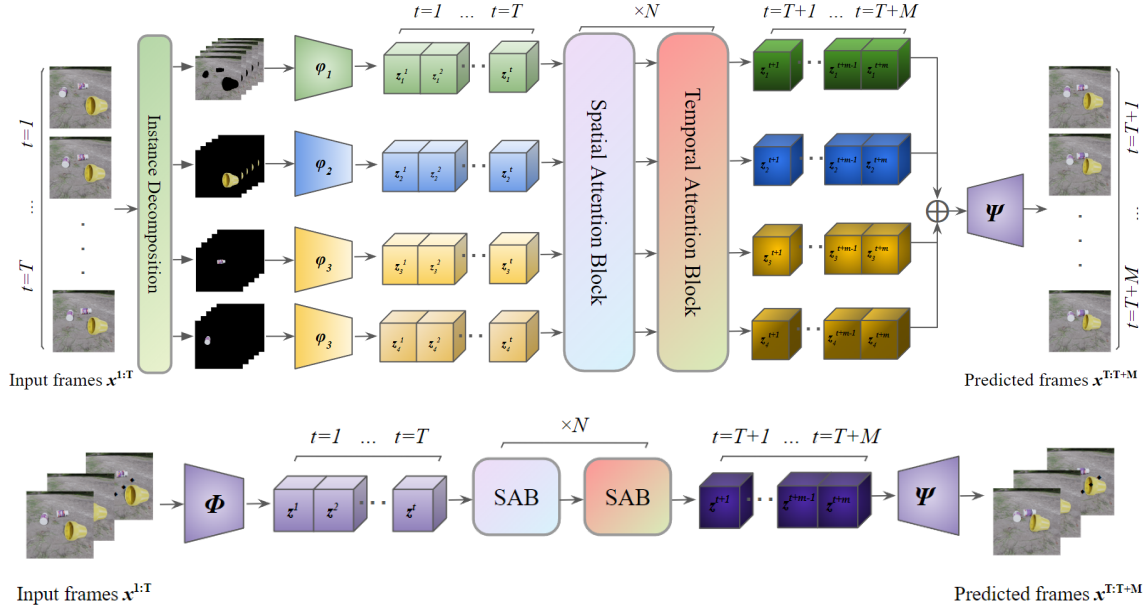


Figure 1: **Top:** Our proposed multi-object interacting model **SCAT**. First the input frames are decomposed via a segmentation model, then each decomposed sequence passes through class-specific encoder to convert the 2D frames into latent representations; then class-specific transformer blocks learn and predict the dynamics of each instance and its relationships with other instances in latent space; lastly, the predicted latent representation are decoded via joint decoder to reconstruct the predicted RGB frames. **Bottom:** The non-decomposed single-slot variant **SiS** where the scene is modeled globally and jointly.

(Reis et al. 2023; Lüddecke and Ecker 2022). The video prediction models then comprise an *object-aware auto-encoder* (OAAE) (Section 3.1), which extracts latent representations for each object, and a multi-object transformer (Section 3.2) that predicts future latent representations conditioned on previous ones; the OAAE is used to decode these future latents back into video frames. To test our hypotheses, we propose three variants of our overall pipeline:

- **Single Slot (SiS):** Objects are not modeled separately; frames are encoded with a single encoder, and a standard (not object-centric) transformer network is used to predict future frames; this is similar to VideoGPT (Yan et al. 2021).
- **Stochastic non-Class Attended Transformer (SNCAT):** The scene is decomposed into instances; both the encoder and predictor have one slot for each object in the scene, with parameters shared across instances of the same class, and no interactions among different object slots in the transformer.
- **Stochastic Class Attended Transformer (SCAT):** Our full model, which encodes instances separately, then uses a multi-slot transformer for future prediction, with cross-attention to capture object interactions.

The overall pipeline of the fully-interacting decomposed **SCAT** and single slot **SiS** models are shown in Figure 1.

### 3.1 Object-aware autoencoder

We now discuss the encoder we use for extracting the latent representation of a video, which will be used in Section 3.2

as a lower-dimensional space for future prediction. We first explain the object-aware autoencoder (OAAE) as used in the **SCAT** and **SNCAT** models, then give a brief explanation of the simpler (non-object-centric) variant used in **SiS**.

**Instance decomposition** Let  $x \in \mathbb{R}^{h \times w \times 3}$  be a frame in an RGB video sequence of width  $w$  and height  $h$ . It is decomposed into a set of instances categorized with corresponding class labels using a segmentation model (Reis et al. 2023; Lüddecke and Ecker 2022). After passing the frame to the segmentation model, the segmentor returns a non-overlapping binary mask for each instance  $k$ , each belonging to one class  $c_k \in \{1, \dots, m\}$ ; we then multiply the input frame by the respective masks to isolate each object. The  $k^{\text{th}}$  masked instance is denoted by  $\tilde{x}_k$  for  $k \in \{1, 2, \dots, N\}$ , and its class is denoted as  $c_k$ . Assuming the segmentation is panoptic and covers all pixels of the frame, the original frame can be reconstructed by recombining all instances of all classes additively as follows:

$$x = \sum_{k=1}^N \tilde{x}_k \quad (1)$$

**Instance embedding** We modify the standard VQ-VAE (van den Oord, Vinyals, and Kavukcuoglu 2017) model to have a set of encoders  $\Phi = \{\phi_1, \phi_2, \dots, \phi_m\}$  and a set of embedding code books  $E = \{e_1, e_2, \dots, e_m\}$ , each associated with an individual semantic class. Each instance frame  $\tilde{x}_k$  is passed to the corresponding encoder  $\phi_{c_k}$  and quantized with  $e_{c_k}$  to produce a latent vector  $\tilde{z}_k$ :

$$\tilde{z}_k = e_{c_k}^i \text{ where } i = \arg \min_j (\|\phi_{c_k}(\tilde{x}_k) - e_{c_k}^j\|_2) \quad (2)$$

The quantized representations are then concatenated into a single vector  $z = \bigoplus_{k=1}^N \tilde{z}_k$  that encodes the complete frame  $x$ . For convenience, we will use the notation  $z = \Phi(x)$  to denote this encoding operation. This latent representation  $z$  is passed to a single joint decoder  $\Psi$  to reconstruct the full frame, i.e.  $\hat{x} = \Psi(z)$ . After each up-sampling convolutional layer in the decoder, we incorporate Frequency Complement Modules (FCM) (Lin et al. 2023) to learn not only from the target frame but also from feature maps between encoder and decoder.

**Loss function** Since our OAAE is a multi-object extended version of the original VQ-VAE (van den Oord, Vinyals, and Kavukcuoglu 2017) with some features of FA-VAE (Lin et al. 2023), we also extend the original loss functions correspondingly. There are 4 losses: feature loss, commitment loss, vector quantisation loss (VQ loss) and reconstruction loss. Following (Lin et al. 2023), we impose a loss on feature maps, not only on the final pixels; similar to them we use focal frequency loss (FFL (Jiang et al. 2021)) between the output of encoder convolution layers and decoder FCM layers:

$$\mathcal{L}_{feature} = \sum_{c=1}^m \sum_{l=0}^{L-1} FFL(f_l^c, g_{L-l}) \quad (3)$$

where  $c$  indexes encoders (recall there is one per class),  $l$  indexes over convolutional layers in the  $c^{\text{th}}$  encoder and  $L-l$  over corresponding FCM layers in the decoder ( $L$  is the total number of decoder layers).  $f_l$  represents the feature map of the  $l^{\text{th}}$  encoder layer, and  $g_l$  that of the  $l^{\text{th}}$  FCM module in the decoder. The VQ and commitment losses are similar to the original VQ-VAE, except we compute these for each class  $c$  and instance  $k$  then sum over these:

$$\mathcal{L}_{VQ} = \sum_{c=1}^m \sum_{k=1}^{n_c} \|\text{sg}[\tilde{z}_k^c] - e_c\|_2^2 \quad (4)$$

$$\mathcal{L}_{commitment} = \sum_{c=1}^m \sum_{k=1}^{n_c} \|\tilde{z}_k^c - \text{sg}[e_c]\|_2^2 \quad (5)$$

where  $\text{sg}$  is the stop-gradient operator. Finally, the reconstruction loss is composed of pixel-space and frequency-space terms calculated between the reconstructed and original frames:

$$\mathcal{L}_{recon} = -\log p(x|\Psi(\Phi(x))) + FFL(x, \Psi(\Phi(x))) \quad (6)$$

Putting all four terms together yields the final loss function for training OAAE:

$$\mathcal{L}_{oaae} = \mathcal{L}_{recon} + \alpha \mathcal{L}_{feature} + \mathcal{L}_{VQ} + \beta \mathcal{L}_{commitment} \quad (7)$$

where  $\alpha$  and  $\beta$  weight the different loss terms. Once the OAAE is trained, we denote the latent representation for the frame  $x^t$  at time step  $t$  as  $z^t$ . This provides a structured and disentangled representation, capturing  $N$  instances across  $m$  classes.

**Variations of the OAAE** In order to measure whether object decomposition helps with prediction, we also define a non-decomposed version of the VQ-VAE, for use in model

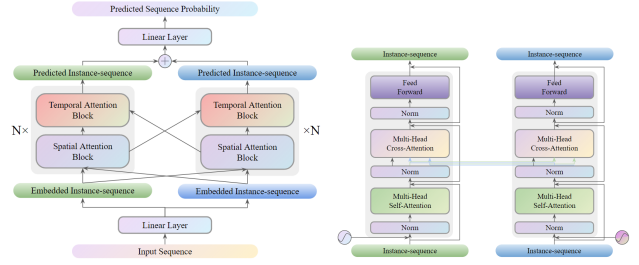


Figure 2: **Left:** Architecture of the multi-object latent transformer. **Right:** Detail of spatial and temporal attention blocks.

**SiS.** This only takes the original non-segmented frame as input. It is processed by a single encoder, with the latent size matched to the total latent size (over all instances) for model **SCAT**. In terms of losses,  $\mathcal{L}_{recon}$  remains unchanged,  $\mathcal{L}_{VQ}$ ,  $\mathcal{L}_{commitment}$  and  $\mathcal{L}_{feature}$  will be a modified to a single term without summation since there is now a single encoder and codebook, and feature maps from just one instance. For the **SNCAT** model variant, the OAAE is identical to the main version for **SCAT**, only the subsequent transformer stage is different.

### 3.2 Prediction Model

Using the OAAE, a video clip  $X$  is encoded as a sequence of latent representations  $Z = \langle z^1, z^2, \dots, z^T \rangle$ . To learn the instance dynamics and its relationship with other instances, we modify the original decoder-only transformer (Vaswani et al. 2017; Radford et al. 2018) into a slot-per-instance auto-regressive transformer that has cross-attention between instances, and shares parameters across instances of each class.

Our transformer consists of alternating attention and feed-forward blocks. However, unlike typical 1D transformers, it includes factored spatial and temporal attention blocks; each of these is applied both for self-attention (i.e. each instance independently attending to other locations / time-points of itself), and cross-attention (i.e. each instance attending to different locations / time-points of all other instances). We use PreNorm (Xiong et al. 2020) in each transformer block. The output vectors for each instance from the last transformer layer are concatenated and passed through a linear layer. The output size matches the number of embeddings in OAAE, allowing the model to predict the probability of possible indices of future frames.

Because the latent vectors produced by the OAAE are a concatenation of each object instance’s latent encoding, we can write the sequence of latent encodings in the video for each individual object instance as  $\tilde{Z}_k = \langle z_k^1, z_k^2, \dots, z_k^T \rangle$  where  $k$  is the  $k_{\text{th}}$  instance.

#### Spatial and temporal extensions of attention layers

Since an instance latent sequence  $\tilde{Z}_k$  has a 3-dimensional shape  $t \times (h \times w) \times c$ , where  $c$  represents embedding dimension in OAAE, it encompasses both temporal and spatial information. Merely flattening the latent vector to form the video sequence in latent space risks losing crucial spa-

tial details. Hence, inspired by (Sun et al. 2023), all attention layers are applied in both spatial ( $h \times w$ ) and temporal  $t$  dimensions. This ensures the model can capture not only the temporal relationships within the sequence but also the important spatial information embedded within each latent representation.

**Instance-level self-attention** For each latent instance frame  $z_k^t$  in the sequence, we first apply learnable positional embeddings. This embedding is added to the input features prior to self-attention to provide the model with information about the position of each instance within the sequence. Scaled self-attention is then applied to each instance sequence separately in order to learn instance-specific dynamics:

$$\text{SA}_c(\tilde{Z}_k) = \text{softmax} \left( \frac{Q_k K_k^T}{\sqrt{d_k}} \right) V_k \quad (8)$$

where SA denotes instance-specific self-attention for objects of class  $c$ ,  $Q_k, K_k^T$ , which  $T$  denotes transpose, and  $V_k$  are the key, query and value calculated by a linear function on  $\tilde{Z}_k$ ;  $\frac{1}{\sqrt{d_k}}$  is a scaling factor that prevents excessively large values in the attention score. Following self-attention, we apply a further linear projection layer.

**Instance-level cross-attention** After the self-attention layer that treats each instance separately, we apply cross-attention between instances to learn the potential relationships and interactions between objects. In this layer, each instance attend the space/time dimensions of each of the other instances:

$$\text{CA}(\tilde{Z}_k) = \bigoplus_{i=1 \dots N, i \neq k} \text{softmax} \left( \frac{Q_k K_i^T}{\sqrt{d_k}} \right) V_i \quad (9)$$

Here CA denotes the cross-attention operation between instance  $k$  and the remaining instances. The value  $V_i$  and key  $K_i$  are derived from  $\tilde{Z}_i$ , while the query originates from  $\tilde{Z}_k$ . The cross-attention layer’s output, being  $n - 1$  times larger than the input because of concatenation, is reduced to the original size through a linear layer.

**Training and inference** The model outputs probabilities over the codebook indices from OAAE, and we use cross-entropy loss to minimize the difference between the predicted and actual distributions. During training, all model variants are trained with teacher forcing on 10-frame clips. Before the forward pass, 10% noise sampled from a standard normal distribution  $\mathcal{N}(0, 1)$  is added to the input frames. During inference, autoregressive sampling is used, starting from an initial sequence of conditioning frames, with softmax temperature treated as a hyperparameter.

**Variants of the transformer** We have described the transformer as used in the full model **SCAT**. In the non-interacting model **SNCAT**, cross-attention is simply replaced by a per-object feed-forward network of similar capacity. The single-slot version **SiS** has a single, larger latent vector for the whole scene instead of separate latents for each object, and we also increase the hidden dimensionality of the transformer (in fact resulting in considerably more

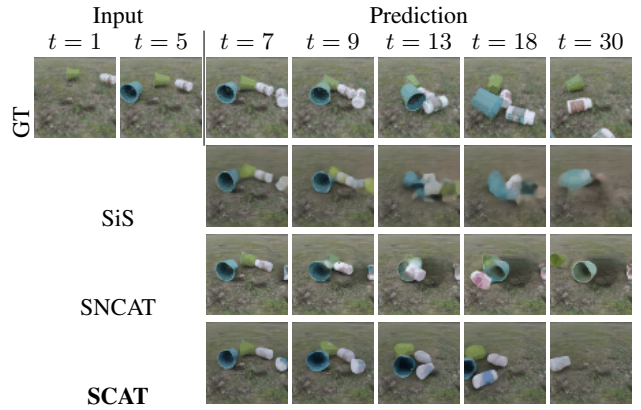


Figure 3: Comparison of different model variants on the **Kubric-Real** dataset. SCAT successfully predicted that the blue pot bounced away whereas SNCAT neglected the interaction between other objects and let the blue pot go through from other objects. The single-slot model SiS fails to capture the appearances well, yielding indistinct predictions for later frames.

parameters). The number of feed-forward and self-attention layers remains the same.

## 4 Experiments

We perform a series of experiments to measure the benefit of separately modeling the dynamics of objects during video prediction. Our focus is on comparing different model variants in a controlled setting, keeping model capacity approximately equal but changing whether the latent representation is decomposed over objects, and whether interactions between objects are modelled if so. In addition, to place our results in context, we perform a comparative evaluation against other recent video prediction models under similar conditions.

**Experimental protocol** Each model is given five frames as input, then predicts the following 5–25 frames depending on the dataset. We use  $64 \times 64$  resolution for all datasets; further details on hyperparameters are in the appendix. The models are implemented in PyTorch and trained on a single NVIDIA RTX 3090 GPU, reflecting our emphasis on computational efficiency and model scalability; further implementation details are given in the appendix. To ensure a rigorous comparison that focuses on the benefit of instance decomposition, we ensure the numbers of parameters in each model are as similar as possible. Our focus is not on achieving state-of-the-art performance but rather on analyzing the benefits of explicit object-centric modeling within a balanced and controlled setting. For quantitative results, we measure LPIPS (Zhang et al. 2018), PSNR (Horé and Ziou 2010) and SSIM (Wang et al. 2004). For brevity we report only average results in the main paper, and provide standard deviations in the appendix.

**Datasets** We conduct experiments on five different datasets characterized by weak and strong interactions. We define weak interactions as scenarios where the dynamics

Table 1: Quantitative results on **KTH** and **Real-Traffic** datasets

	<b>KTH</b>				<b>Real-Traffic</b>			
	PSNR $\uparrow$	SSIM $\uparrow$	LPIPS $\downarrow$	Num-Prms	PSNR $\uparrow$	SSIM $\uparrow$	LPIPS $\downarrow$	Num-Prms
Single-Slot	25.26	0.765	0.110	48M	28.34	0.933	0.026	286M
SNCAT	25.39	0.768	0.112	25M	28.85	0.942	0.020	27M
SCAT	<b>25.61</b>	<b>0.774</b>	<b>0.108</b>	23M	<b>30.04</b>	<b>0.947</b>	<b>0.017</b>	28M

Table 2: Quantitative results on **CLEVR-2**, **CLEVR-3**, and **Kubric-Real** datasets

	<b>CLEVR-2</b>				<b>CLEVR-3</b>				<b>Kubric-Real</b>			
	PSNR $\uparrow$	SSIM $\uparrow$	LPIPS $\downarrow$	Num-Prms	PSNR $\uparrow$	SSIM $\uparrow$	LPIPS $\downarrow$	Num-Prms	PSNR $\uparrow$	SSIM $\uparrow$	LPIPS $\downarrow$	Num-Prms
Single-Slot	<b>30.16</b>	<b>0.906</b>	0.061	105M	30.15	0.895	0.068	186M	22.88	0.729	0.165	287M
SNCAT	28.19	0.887	0.110	25M	28.01	0.879	0.104	26M	22.89	0.743	0.156	38M
SCAT	30.03	0.905	<b>0.056</b>	25M	<b>32.25</b>	<b>0.925</b>	<b>0.030</b>	26M	<b>24.15</b>	<b>0.773</b>	<b>0.122</b>	40M

of an instance are unaffected by other instances, or minimally so. In contrast, strong interactions involve instances significantly affecting each other’s dynamics, such as during collisions.

The first weak interaction dataset we use is the **KTH** human action dataset (Schuldt, Laptev, and Caputo 2004). This includes six action types performed by 25 individuals. Although the primary focus is on the person, there remains some slight interaction between the person and the background, such as shadows cast by the individual on the background. Following MOSO (Sun et al. 2023), we use videos of persons 1-16 for training and 17-25 for testing. We used (Lüddecke and Ecker 2022) to segment the person and the background. Each model is given five frames and required to predict 15 future frames. The second weak interaction dataset is the **Real-Traffic** dataset from (Ehrhardt et al. 2020). This comprises video clips taken from a CCTV camera overlooking a highway intersection. The background is static, and only the cars are moving in the scene; there are up to five cars per clip. The original dataset contains 615 video clips with various lengths, we split the dataset into a more standardized 10 frames per clip with 5089 clips for training and 2181 for validation. During inference the models are given five frames and required to predict five future frames. We used YOLOv8 (Reis et al. 2023) to extract each instance. Each car’s motion is independent of other cars most of the time; however, interactions do occur, such as when a car stops before the intersection, causing other cars behind it to slow down. For quantitative evaluation, we therefore identify a subset of video clips from the test set with the strongest interactions. We calculate the distances between centroids of different cars, and select clips where the distance between any pair of cars is less than 25% of the image size; this yields a test set of 807 clips.

For strong interaction datasets, we used Kubric (Greff et al. 2022) to generate a series of synthetic datasets inspired by CLEVRER (Yi et al. 2019) but exhibiting stronger interactions and more visual complexity. Full details on the dataset generation (and corresponding code) are included in the appendix. Specifically, **CLEVR-2** contains scenes with two spheres with random velocity sampled such that they will collide; **CLEVR-3** scenes are similar but include an-

other sphere that does not interact with the first two. **Kubric-Real** uses a realistic background and replaces the basic geometric objects with 3D-scanned objects—bottles and pots since these exhibit interesting dynamics due to their cylindrical shapes.

**Internal and External Evaluation** We first compare the different variations of our model, to evaluate the benefit of explicit object-centric modeling in a controlled setting. Table 1 shows quantitative results on the two weak-interaction datasets. For **KTH**, the models are given five frames and required to predict 15 frames and for **Real-Traffic** they are required to predict five frames. In both datasets the proposed model performs best among other two variations. First, modeling the scene separately by segmenting it at the instance level (SNCAT) leads to predictions comparable to modeling the whole scene at once (Single-slot model), while using a much smaller model (25M vs. 48M parameters on **KTH**, 27M vs. 286M parameters on **Real-Traffic**). Second, adding cross-attention to the model to handle potential interactions between instances (SCAT) leads to an improvement in performance across all metrics. Since **KTH** features a single instance with negligible interaction, the performance improvement is subtle on each metric: SSIM (+0.006), PSNR (+0.35) and LPIPS (-0.02). On **Real-Traffic**, which has more instances and higher interactions, consistent improvements are observed in all metrics (PSNR: +1.70, SSIM: +0.014, LPIPS: -0.009). These results confirm the computational advantage of both the decomposition and cross-attention components of the approach. Table 2 provides quantitative results on the strong-interaction datasets. On **CLEVR-2**, the SCAT model (PSNR: 30.03) performs similarly to the single-slot model (PSNR: 30.16) but outperforms it on LPIPS (0.056 vs. 0.061). In contrast, SNCAT performs worse than the single-slot model both on **CLEVR-2** and **CLEVR-3** datasets, this due to the lack of cross-attention to model interactions between objects. In **Kubric-Real**, SNCAT preserves object shapes better than the single-slot model, which struggles with deformation after collision. SCAT outperforms both models in LPIPS (0.122 vs. 0.165 for the single-slot model) and SSIM (0.773 vs. 0.729 for the single-slot model), emphasizing the importance of cross-

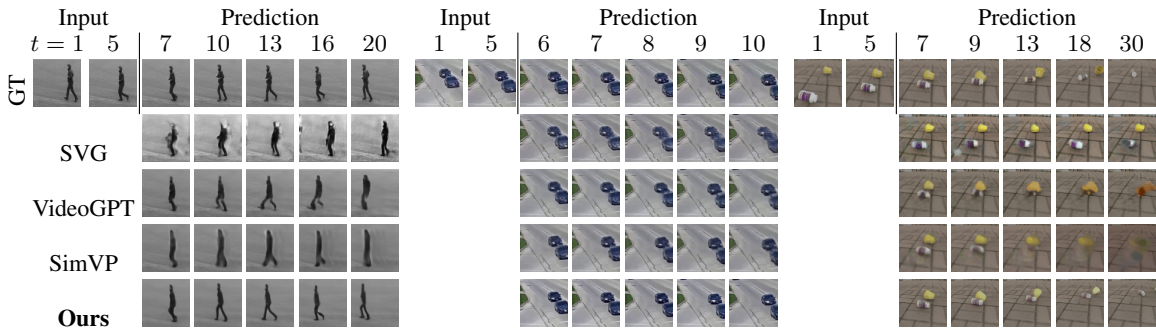


Figure 4: Qualitative results from our full model and baselines on **KTH** (left), **Real-Traffic** (middle) and **Kubric-real** (right).

Table 3: Quantitative results on **KTH**, **Real-Traffic** and **Kubric-Real** datasets

	<b>KTH</b>				<b>Real-Traffic</b>				<b>Kubric-Real</b>			
	PSNR $\uparrow$	SSIM $\uparrow$	LPIPS $\downarrow$	Num-Prms	PSNR $\uparrow$	SSIM $\uparrow$	LPIPS $\downarrow$	Num-Prms	PSNR $\uparrow$	SSIM $\uparrow$	LPIPS $\downarrow$	Num-Prms
SVG	16.27	0.572	0.160	23M	23.67	0.893	0.101	31M	15.48	0.615	0.720	41M
VideoGPT	24.39	0.788	<b>0.086</b>	41M	29.19	0.928	0.023	55M	23.68	0.702	0.153	67M
SimVP	25.45	<b>0.810</b>	0.117	56M	<b>30.51</b>	<b>0.949</b>	0.019	31M	22.21	0.711	0.213	59M
SCAT	<b>25.52</b>	0.774	0.108	23M	30.04	0.947	<b>0.017</b>	28M	<b>24.15</b>	<b>0.773</b>	<b>0.122</b>	40M

attention in more realistic and complex interaction scenes. These results confirm our hypothesis that instance segmentation is important for video prediction and that cross-attention is an effective way to encode strong interactions. Moreover, without cross-attention, instance separation on its own is sufficient to achieve similar or better performance compared to the baseline single-slot model on complex scenes (**Real-traffic**, **Kubric-Real**) having more than two instances, with only a fraction of the parameters. Although the main focus of our work is on measuring the benefit of object-centric video modeling in a controlled setting, we also compare our method with other similar state-of-the-art methods to better contextualize those results. Our model is designed to be small yet efficient, demonstrating high performance without the need for large-scale resources. In contrast, many existing models rely on significantly larger architectures to achieve similar results, which can be resource-intensive and less practical. To ensure a fair and balanced evaluation, we therefore adjusted each method’s hyperparameters to match our model’s size (i.e. number of weights), providing a level playing field for comparison. We compare against VideoGPT (Yan et al. 2021), which uses a similar architecture, and the CNN-based SimVP (Gao et al. 2022) for a comprehensive evaluation.

Prediction performance on **KTH**, **Real-Traffic** and **Kubric-Real** are presented in Table 3. The SCAT model outperforms or is competitive with other models across all three datasets, even with its smaller model size, confirming the effectiveness of instance-level segmentation and cross-attention. On the simpler **KTH** dataset, VideoGPT achieves slightly higher SSIM than SCAT (0.788 vs 0.772) and slightly lower LPIPS than SCAT (0.086 vs 0.098), but lower quality according to PSNR (24.39 vs 25.46). Moreover, from Fig.4 we can see that only SCAT maintained human posture throughout the prediction. On **Real-Traffic**, SCAT again achieves competitive performance, with PSNR

of 30.04, which is higher than VideoGPT (29.19) but lower than SimVP (30.51). SCAT performs best under the perceptually robust LPIPS metric (0.017), outperforming both VideoGPT (0.023) and SimVP (0.019), indicating better perceptual quality. Also, from Figure 4 we can see that when  $t=9$  and  $t=10$ , SCAT maintained the distance between two cars and kept them separate while the other models merged two cars. On **Kubric-Real**, where strong interactions and realistic objects are present, our model leads by a large margin on every metric. This further shows the proposed model’s improvement is larger on scenes with more instances and strong interactions. In Figure 4 other methods failed to predict the collision between two objects, while SCAT predicted this accurately and maintained the object shape.

## 5 Conclusion

In this paper, we investigated and analyzed the benefits of explicit object-centric decomposition in video prediction. We proposed a video prediction pipeline based on an object-aware VQ-VAE and multi-object Transformer, that operates on separate objects extracted via panoptic segmentation; we also defined variants that lack object-decomposition and support for interactions. We evaluated the proposed models on five datasets, finding that when a dynamic scene is explicitly decomposed and encoded into a structured latent vector, prediction quality is better than an equal-capacity model without decomposition.

## References

- Bei, X.; Yang, Y.; and Soatto, S. 2021. Learning Semantic-Aware Dynamics for Video Prediction. *CoRR*, abs/2104.09762.
- Blattmann, A.; Dockhorn, T.; Kulal, S.; Mendelevitch, D.; Kilian, M.; Lorenz, D.; Levi, Y.; English, Z.; Voleti, V.;

- Letts, A.; et al. 2023a. Stable video diffusion: Scaling latent video diffusion models to large datasets. *arXiv preprint arXiv:2311.15127*.
- Blattmann, A.; Rombach, R.; Ling, H.; Dockhorn, T.; Kim, S. W.; Fidler, S.; and Kreis, K. 2023b. Align your Latents: High-Resolution Video Synthesis with Latent Diffusion Models. In *IEEE Conference on Computer Vision and Pattern Recognition (CVPR)*.
- Brooks, T.; Peebles, B.; Holmes, C.; DePue, W.; Guo, Y.; Jing, L.; Schnurr, D.; Taylor, J.; Luhman, T.; Luhman, E.; Ng, C.; Wang, R.; and Ramesh, A. 2024. Video generation models as world simulators.
- Chang, Z.; Zhang, X.; Wang, S.; Ma, S.; and Gao, W. 2022. STAM: A SpatioTemporal Attention based Memory for Video Prediction. *IEEE Transactions on Multimedia*, 1–1.
- Denton, E.; and Fergus, R. 2018. Stochastic video generation with a learned prior. In *International conference on machine learning*, 1174–1183. PMLR.
- Denton, E. L.; et al. 2017. Unsupervised learning of disentangled representations from video. *Advances in neural information processing systems*, 30.
- Dosovitskiy, A.; Beyer, L.; Kolesnikov, A.; Weissenborn, D.; Zhai, X.; Unterthiner, T.; Dehghani, M.; Minderer, M.; Heigold, G.; Gelly, S.; et al. 2020. An image is worth 16x16 words: Transformers for image recognition at scale. *arXiv preprint arXiv:2010.11929*.
- Ehrhardt, S.; Groth, O.; Monszpart, A.; Engelcke, M.; Posner, I.; J. Mitra, N.; and Vedaldi, A. 2020. RELATE: Physically Plausible Multi-Object Scene Synthesis Using Structured Latent Spaces. In *Advances in Neural Information Processing Systems (NeurIPS)*.
- Engelcke, M.; Kosiorek, A. R.; Jones, O. P.; and Posner, I. 2019. Genesis: Generative scene inference and sampling with object-centric latent representations. *arXiv preprint arXiv:1907.13052*.
- Esser, P.; Rombach, R.; and Ommer, B. 2021. Taming transformers for high-resolution image synthesis. In *Proceedings of the IEEE/CVF conference on computer vision and pattern recognition*, 12873–12883.
- Gao, Z.; Tan, C.; Wu, L.; and Li, S. Z. 2022. SimVP: Simpler Yet Better Video Prediction. In *Proceedings of the IEEE/CVF Conference on Computer Vision and Pattern Recognition (CVPR)*, 3170–3180.
- Greff, K.; Belletti, F.; Beyer, L.; Doersch, C.; Du, Y.; Duckworth, D.; Fleet, D. J.; Gnanapragasam, D.; Golemo, F.; Herrmann, C.; Kipf, T.; Kundu, A.; Lagun, D.; Laradji, I.; Liu, H.-T. D.; Meyer, H.; Miao, Y.; Nowrouzezahrai, D.; Oztireli, C.; Pot, E.; Radwan, N.; Rebain, D.; Sabour, S.; Sajjadi, M. S. M.; Sela, M.; Sitzmann, V.; Stone, A.; Sun, D.; Vora, S.; Wang, Z.; Wu, T.; Yi, K. M.; Zhong, F.; and Tagliasacchi, A. 2022. Kubric: a scalable dataset generator.
- Gupta, A.; Tian, S.; Zhang, Y.; Wu, J.; Martín-Martín, R.; and Fei-Fei, L. 2022. Maskvit: Masked visual pre-training for video prediction. *arXiv preprint arXiv:2206.11894*.
- He, K.; Gkioxari, G.; Dollár, P.; and Girshick, R. 2017. Mask r-cnn. In *Proceedings of the IEEE international conference on computer vision*, 2961–2969.
- Henderson, P.; and Lampert, C. H. 2020. Unsupervised object-centric video generation and decomposition in 3D. In *Advances in Neural Information Processing Systems (NeurIPS)* 33.
- Henderson, P.; Lampert, C. H.; and Bickel, B. 2021. Unsupervised Video Prediction from a Single Frame by Estimating 3D Dynamic Scene Structure. *arXiv:2106.09051*.
- Ho, J.; Jain, A.; and Abbeel, P. 2020. Denoising diffusion probabilistic models. *Advances in neural information processing systems*, 33: 6840–6851.
- Ho, J.; Salimans, T.; Gritsenko, A.; Chan, W.; Norouzi, M.; and Fleet, D. J. 2022. Video Diffusion Models. In Koyejo, S.; Mohamed, S.; Agarwal, A.; Belgrave, D.; Cho, K.; and Oh, A., eds., *Advances in Neural Information Processing Systems*, volume 35, 8633–8646. Curran Associates, Inc.
- Höppe, T.; Mehrjou, A.; Bauer, S.; Nielsen, D.; and Dittadi, A. 2022. Diffusion models for video prediction and infilling. *arXiv preprint arXiv:2206.07696*.
- Horé, A.; and Ziou, D. 2010. Image Quality Metrics: PSNR vs. SSIM. In *2010 20th International Conference on Pattern Recognition*, 2366–2369.
- Hsieh, J.-T.; Liu, B.; Huang, D.-A.; Fei-Fei, L. F.; and Niebles, J. C. 2018. Learning to Decompose and Disentangle Representations for Video Prediction. In Bengio, S.; Wallach, H.; Larochelle, H.; Grauman, K.; Cesa-Bianchi, N.; and Garnett, R., eds., *Advances in Neural Information Processing Systems*, volume 31. Curran Associates, Inc.
- Jiang, J.; Janghorbani, S.; De Melo, G.; and Ahn, S. 2019. SCALOR: Generative World Models with Scalable Object Representations. In *International Conference on Learning Representations*.
- Jiang, L.; Dai, B.; Wu, W.; and Loy, C. C. 2021. Focal Frequency Loss for Image Reconstruction and Synthesis. In *ICCV*.
- Kipf, T.; Elsayed, G. F.; Mahendran, A.; Stone, A.; Sabour, S.; Heigold, G.; Jonschkowski, R.; Dosovitskiy, A.; and Greff, K. 2021. Conditional object-centric learning from video. *arXiv preprint arXiv:2111.12594*.
- Krizhevsky, A.; Sutskever, I.; and Hinton, G. E. 2012. Imagenet classification with deep convolutional neural networks. *Advances in neural information processing systems*, 25.
- Lee, D.; Lee, J.; and Choi, J. 2023. CAST: Cross-Attention in Space and Time for Video Action Recognition. In Oh, A.; Naumann, T.; Globerson, A.; Saenko, K.; Hardt, M.; and Levine, S., eds., *Advances in Neural Information Processing Systems*, volume 36, 79399–79425. Curran Associates, Inc.
- Lee, W.; Jung, W.; Zhang, H.; Chen, T.; Koh, J. Y.; Huang, T. E.; Yoon, H.; Lee, H.; and Hong, S. 2021. Revisiting Hierarchical Approach for Persistent Long-Term Video Prediction. *CoRR*, abs/2104.06697.

- Li, N.; Raza, M. A.; Hu, W.; Sun, Z.; and Fisher, R. 2021. Object-Centric Representation Learning with Generative Spatial-Temporal Factorization. In Ranzato, M.; Beygelzimer, A.; Dauphin, Y.; Liang, P.; and Vaughan, J. W., eds., *Advances in Neural Information Processing Systems*, volume 34, 10772–10783. Curran Associates, Inc.
- Lin, X.; Li, Y.; Hsiao, J.; Ho, C.; and Kong, Y. 2023. Catch Missing Details: Image Reconstruction with Frequency Augmented Variational Autoencoder. In *Proceedings of the IEEE/CVF Conference on Computer Vision and Pattern Recognition*.
- Liu, Y.; Zhang, K.; Li, Y.; Yan, Z.; Gao, C.; Chen, R.; Yuan, Z.; Huang, Y.; Sun, H.; Gao, J.; et al. 2024. Sora: A review on background, technology, limitations, and opportunities of large vision models. *arXiv preprint arXiv:2402.17177*.
- Locatello, F.; Weissenborn, D.; Unterthiner, T.; Mahendran, A.; Heigold, G.; Uszkoreit, J.; Dosovitskiy, A.; and Kipf, T. 2020. Object-centric learning with slot attention. *Advances in neural information processing systems*, 33: 11525–11538.
- Lüddecke, T.; and Ecker, A. 2022. Image Segmentation Using Text and Image Prompts. In *2022 IEEE/CVF Conference on Computer Vision and Pattern Recognition (CVPR)*, 7076–7086.
- Radford, A.; Narasimhan, K.; Salimans, T.; Sutskever, I.; et al. 2018. Improving language understanding by generative pre-training.
- Ravuri, S.; Lenc, K.; Willson, M.; Kangin, D.; Lam, R.; Mirowski, P.; Fitzsimons, M.; Athanassiadou, M.; Kashem, S.; Madge, S.; et al. 2021. Skilful precipitation nowcasting using deep generative models of radar. *Nature*, 597(7878): 672–677.
- Reis, D.; Kupec, J.; Hong, J.; and Daoudi, A. 2023. Real-time flying object detection with YOLOv8. *arXiv preprint arXiv:2305.09972*.
- Rombach, R.; Blattmann, A.; Lorenz, D.; Esser, P.; and Ommer, B. 2022. High-resolution image synthesis with latent diffusion models. In *Proceedings of the IEEE/CVF conference on computer vision and pattern recognition*, 10684–10695.
- Sajjadi, M. S.; Duckworth, D.; Mahendran, A.; Van Steenkiste, S.; Pavetic, F.; Lucic, M.; Guibas, L. J.; Greff, K.; and Kipf, T. 2022. Object scene representation transformer. *Advances in neural information processing systems*, 35: 9512–9524.
- Schmeckpeper, K.; Georgakis, G.; and Daniilidis, K. 2021. Object-centric video prediction without annotation. In *2021 IEEE International Conference on Robotics and Automation (ICRA)*, 13604–13610. IEEE.
- Schuldt, C.; Laptev, I.; and Caputo, B. 2004. Recognizing human actions: a local SVM approach. In *Proceedings of the 17th International Conference on Pattern Recognition, 2004. ICPR 2004.*, volume 3, 32–36. IEEE.
- Shi, T.; Ge, X.; Jose, J. M.; Pugeault, N.; and Henderson, P. 2024. Detail-Enhanced Intra-and Inter-modal Interaction for Audio-Visual Emotion Recognition. *arXiv preprint arXiv:2405.16701*.
- Shi, X.; Chen, Z.; Wang, H.; Yeung, D.-Y.; Wong, W.-K.; and Woo, W.-c. 2015. Convolutional LSTM network: A machine learning approach for precipitation nowcasting. *Advances in neural information processing systems*, 28.
- Singh, G.; Wu, Y.-F.; and Ahn, S. 2022. Simple unsupervised object-centric learning for complex and naturalistic videos. *Advances in Neural Information Processing Systems*, 35: 18181–18196.
- Sohl-Dickstein, J.; Weiss, E.; Maheswaranathan, N.; and Ganguli, S. 2015. Deep Unsupervised Learning using Nonequilibrium Thermodynamics. In Bach, F.; and Blei, D., eds., *Proceedings of the 32nd International Conference on Machine Learning*, volume 37 of *Proceedings of Machine Learning Research*, 2256–2265. Lille, France: PMLR.
- Sun, M.; Wang, W.; Zhu, X.; and Liu, J. 2023. MOSO: Decomposing MOtion, Scene and Object for Video Prediction. *arXiv:2303.03684*.
- van den Oord, A.; Vinyals, O.; and Kavukcuoglu, K. 2017. Neural Discrete Representation Learning. In Guyon, I.; Luxburg, U. V.; Bengio, S.; Wallach, H.; Fergus, R.; Vishwanathan, S.; and Garnett, R., eds., *Advances in Neural Information Processing Systems*, volume 30. Curran Associates, Inc.
- Vaswani, A.; Shazeer, N.; Parmar, N.; Uszkoreit, J.; Jones, L.; Gomez, A. N.; Kaiser, Ł.; and Polosukhin, I. 2017. Attention is all you need. *Advances in neural information processing systems*, 30.
- Villar-Corrales, A.; Wahdan, I.; and Behnke, S. 2023. Object-Centric Video Prediction Via Decoupling of Object Dynamics and Interactions. In *2023 IEEE International Conference on Image Processing (ICIP)*, 570–574.
- Wang, X.; Zhu, Z.; Huang, G.; Wang, B.; Chen, X.; and Lu, J. 2024. Worlddreamer: Towards general world models for video generation via predicting masked tokens. *arXiv preprint arXiv:2401.09985*.
- Wang, Y.; Gao, Z.; Long, M.; Wang, J.; and Philip, S. Y. 2018. Predrnn++: Towards a resolution of the deep-in-time dilemma in spatiotemporal predictive learning. In *International Conference on Machine Learning*, 5123–5132. PMLR.
- Wang, Y.; Wu, H.; Zhang, J.; Gao, Z.; Wang, J.; Yu, P.; and Long, M. 2022. PredRNN: A recurrent neural network for spatiotemporal predictive learning. *IEEE Transactions on Pattern Analysis and Machine Intelligence*.
- Wang, Z.; Bovik, A.; Sheikh, H.; and Simoncelli, E. 2004. Image quality assessment: from error visibility to structural similarity. *IEEE Transactions on Image Processing*, 13(4): 600–612.
- Wu, J.; Yin, S.; Feng, N.; He, X.; Li, D.; Hao, J.; and Long, M. 2024. iVideoGPT: Interactive VideoGPTs are Scalable World Models. *arXiv preprint arXiv:2405.15223*.
- Wu, Z.; Dvornik, N.; Greff, K.; Kipf, T.; and Garg, A. 2022. Slotformer: Unsupervised visual dynamics simulation with object-centric models. *arXiv preprint arXiv:2210.05861*.
- Xiong, R.; Yang, Y.; He, D.; Zheng, K.; Zheng, S.; Xing, C.; Zhang, H.; Lan, Y.; Wang, L.; and Liu, T. 2020. On

layer normalization in the transformer architecture. In *International Conference on Machine Learning*, 10524–10533. PMLR.

Yan, W.; Zhang, Y.; Abbeel, P.; and Srinivas, A. 2021. Videogpt: Video generation using vq-vae and transformers. *arXiv preprint arXiv:2104.10157*.

Yang, J.; Gao, S.; Qiu, Y.; Chen, L.; Li, T.; Dai, B.; Chitta, K.; Wu, P.; Zeng, J.; Luo, P.; Zhang, J.; Geiger, A.; Qiao, Y.; and Li, H. 2024. Generalized Predictive Model for Autonomous Driving. In *Proceedings of the IEEE/CVF Conference on Computer Vision and Pattern Recognition (CVPR)*, 14662–14672.

Yi, K.; Gan, C.; Li, Y.; Kohli, P.; Wu, J.; Torralba, A.; and Tenenbaum, J. B. 2019. Clevrer: Collision events for video representation and reasoning. *arXiv preprint arXiv:1910.01442*.

Yu, S.; Sohn, K.; Kim, S.; and Shin, J. 2023. Video probabilistic diffusion models in projected latent space. In *Proceedings of the IEEE/CVF conference on computer vision and pattern recognition*, 18456–18466.

Zhang, R.; Isola, P.; Efros, A. A.; Shechtman, E.; and Wang, O. 2018. The unreasonable effectiveness of deep features as a perceptual metric. In *Proceedings of the IEEE conference on computer vision and pattern recognition*, 586–595.

Zhou, Y.; Zhang, H.; Lee, H.; Sun, S.; Li, P.; Zhu, Y.; Yoo, B.; Qi, X.; and Han, J.-J. 2022. Slot-vps: Object-centric representation learning for video panoptic segmentation. In *Proceedings of the IEEE/CVF Conference on Computer Vision and Pattern Recognition*, 3093–3103.

Zhu, H.; Ke, W.; Li, D.; Liu, J.; Tian, L.; and Shan, Y. 2022. Dual Cross-Attention Learning for Fine-Grained Visual Categorization and Object Re-Identification. In *Proceedings of the IEEE/CVF Conference on Computer Vision and Pattern Recognition (CVPR)*, 4692–4702.

## Implementation Details

Specific implementation details of both **Object Aware Auto-Encoder (OAAE)**, **Stochastic Class-Attended Transformer (SCAT)** and their variants are given in table 4 and 5. We ensured that the non-decomposed version was fairly compared to the decomposed version by adjusting the embedding dimensions accordingly. Specifically, the embedding dimension in the non-decomposed version was set to be  $N$  times larger than the embedding dimension of a single instance in the decomposed setting, where  $N$  represents the total number of instances. For example, in the **Kubric-Real** dataset, there are three classes: background, bottles, and pots. The background class is assigned one slot, the bottles class is assigned two slots, and the pots class is assigned two slots, totaling five instances. Thus, if each instance in the decomposed version has an embedding dimension of 128, then in the non-decomposed version, the embedding dimension is set to 640, which is 128 multiplied by the total number of instances (5).

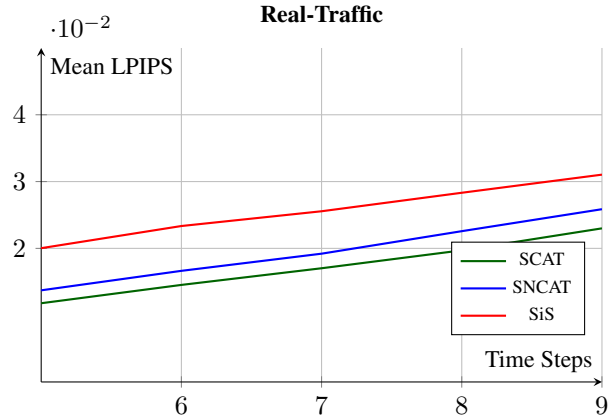


Figure 5: Comparison of Mean LPIPS Values on **Real-Traffic** datasets

## Dataset Details

**Decomposition** For KTH, we use CLIPSeg with the prompt ‘person’ and ‘background’ to decompose the frames. For Real-Traffic, we use YOLOv8 to be our instance segmentor. For Kubric generated datasets, because the instance segmentation map is available with the generation, we directly use these to extract the instances.

**Synthetic Datasets Generation** We use Kubric to generate **CLEVR-2**, **CLEVR-3** and **Kubric-Real**. Generation parameters are given in Table 6. The table outlines the parameters for generating the CLEVR-2, CLEVR-3, and Kubric-Real datasets. All three datasets use a colliding position range of  $[-1, 1]$  and a fixed, static camera looking at  $(0, 0)$ . The summoning radius is set to 5 for CLEVR datasets and 8 for Kubric-Real, with minimum summoning distances of 2 for CLEVR and 4 for Kubric-Real. CLEVR datasets feature object friction values of 0.4 for metal spheres and 0.8 for rubber spheres, while Kubric-Real has a uniform friction of 1.0. This higher friction in Kubric-Real necessitates a larger maximum initial velocity of 7, compared to 5 in the CLEVR datasets. The number of objects also increases from 2 in CLEVR-2 to 3 in CLEVR-3, and 4 in Kubric-Real. More details are given in table 6.

## More Results

Here we illustrate the quantitative results of our models on each datasets. The results are produced by sampling using set of 10 temperature values from 0.1 to 0.9 meaning that lower to higher stochasticity, then the best result is selected to compare. Each dataset’s testing set is divided into 10 subsets. First, the mean of each metric on the subset is calculated, then the overall mean and std is calculated using 10 mean values accordingly. On **Kubric-Real** dataset, by reaching the end of prediction **SCAT** and **SNCAT** starts to predict better. This is because in the ground truth, the objects are either no longer in the scene or staying still.

	<b>KTH</b>		<b>Real-Traffic</b>		<b>CLEVR-2</b>		<b>CLEVR-3</b>		<b>Kubric-Real</b>	
	OAAE	Non-Decom	OAAE	Non-Decom	OAAE	Non-Decom	OAAE	Non-Decom	OAAE	Non-Decom
In Channels	1		3		3		3		3	
Num Instance	2	1	5	1	3	1	4	1	5	1
Num Classes	2	1	2	1	2	1	2	1	3	1
Embedding Dim Per Instance	128	256	128	640	128	384	128	512	128	640
Num Embeddings	5120		5120		5120		5120		5120	
Conv Hidden Dims	128, 256		128, 256		128, 256		128, 256		128, 256	
Num Residual Layers	6		6		6		6		6	
Batch Size	8		8		8		8		8	
Learning Rate	$10^{-4}$		$10^{-4}$		$10^{-4}$		$10^{-4}$		$10^{-4}$	

Table 4: HyperParameters of OAAE on **KTH**, **Real-Traffic**, **CLEVR-2**, **CLEVR-3** and **Kubric-Real** Datasets

	<b>KTH</b>			<b>Real-Traffic</b>			<b>CLEVR-2</b>			<b>CLEVR-3</b>			<b>Kubric-Real</b>		
	SCAT	SNCAT	SiS	SCAT	SNCAT	SiS	SCAT	SNCAT	SiS	SCAT	SNCAT	SiS	SCAT	SNCAT	SiS
Num Instance	2	1	5	1	3	1	4	1	5	1					
Num Classes	2	1	2	1	2	1	2	1	3	1					
VQVAE Dim	128	256	128	640	128	384	128	512	128	640					
Embedding Dim Per Instance	256	512	256	1280	256	768	256	1024	256	1280					
Num Attention Head	16			16			16			16					
FeedForward expanding Factor	2			2			2			2					
Depth	4			4			4			4					
Drop Out	0.3			0.3			0.3			0.3					
Batch Size	1			1			1			1					
Learning Rate	$10^{-4}$			$10^{-4}$			$10^{-4}$			$10^{-4}$					
LR Scheduler	Cosine			Cosine			Cosine			Cosine					
Warm-up Steps	10000			10000			10000			10000					

Table 5: HyperParameters of SCAT and its variants on **KTH**, **Real-Traffic**, **CLEVR-2**, **CLEVR-3** and **Kubric-Real** Datasets

	<b>CLEVR-2</b>	<b>CLEVR-3</b>	<b>Kubric-Real</b>
Colliding Position Range ( $x, y$ )	[-1,1]	[-1,1]	[-1,1]
Radius for Summoning Objects	5	5	8
Min Distance When Summoning	2	2	4
Max Initial Velocity	5	5	7
Ground Friction	0.3	0.3	0.3
Object Friction	0.4,0.8	0.4,0.8	1.0
Num Objects	2	3	4
Num Object Class	1	1	2
Camera Position	Fixed Static	Fixed Static	Fixed Static
Camera Looks At ( $x, y, z$ )	(0, 0, 0)	(0, 0, 0)	(0, 0, 0)

Table 6: Parameters for Generating **CLEVR-2**, **CLEVR-3** and **Kubric-Real** Datasets

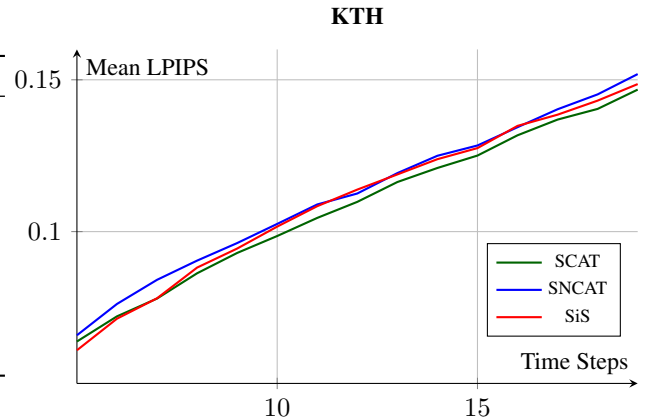


Figure 6: Comparison of Mean LPIPS Values on **KTH** datasets

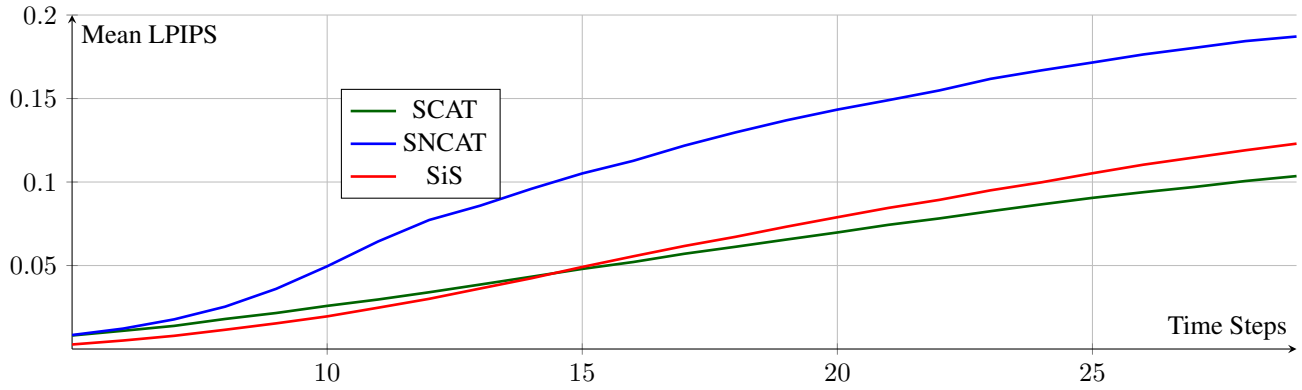


Figure 7: Comparison of Mean LPIPS Values on **CLEVR-2** dataset

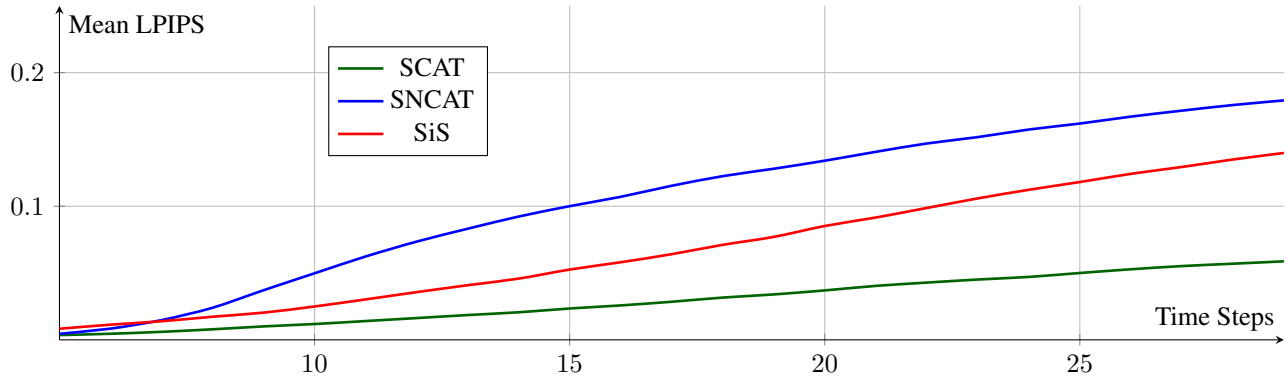


Figure 8: Comparison of Mean LPIPS Values on **CLEVR-3** dataset

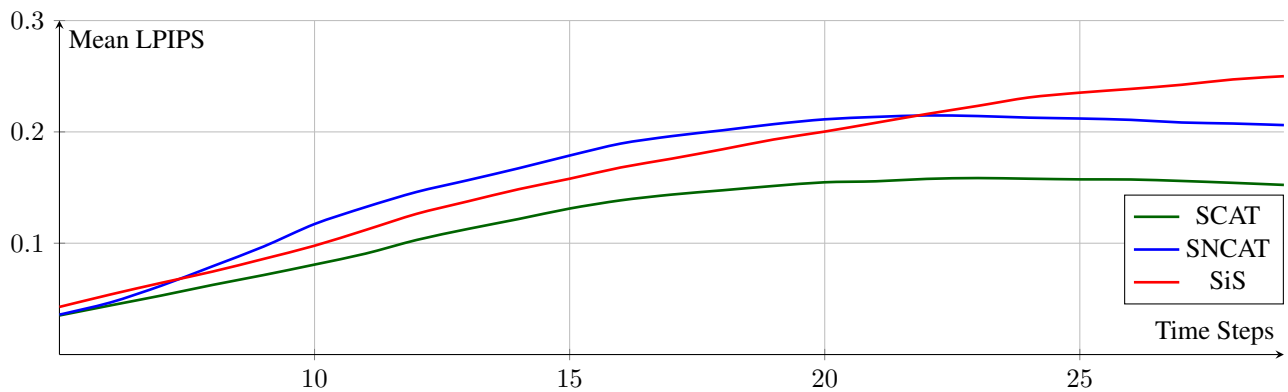


Figure 9: Comparison of Mean LPIPS Values on **Kubric-Real** dataset

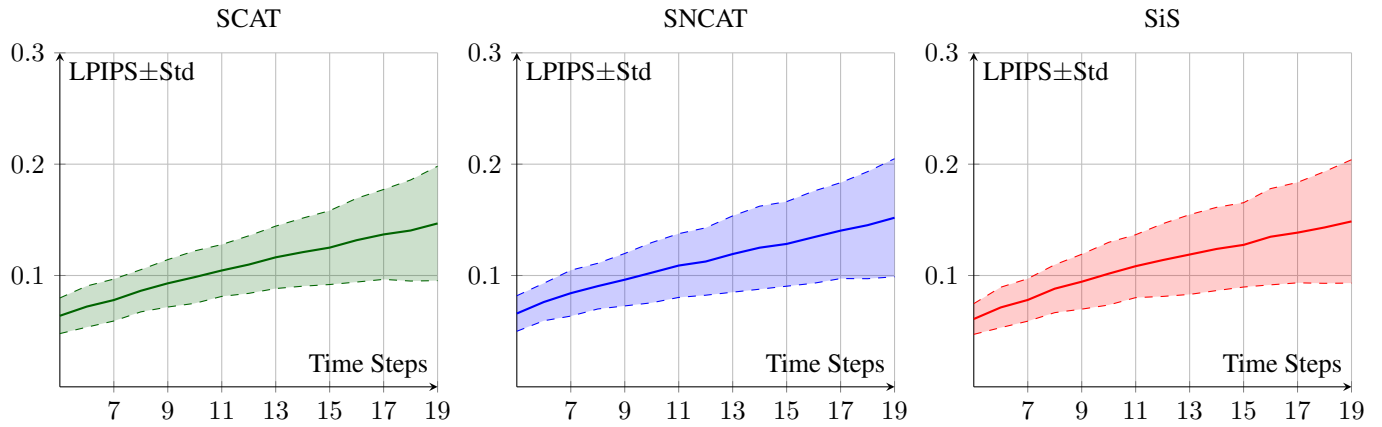


Figure 10: Mean and Std (Standard Deviation) of LPIPS metric on **KTH** dataset

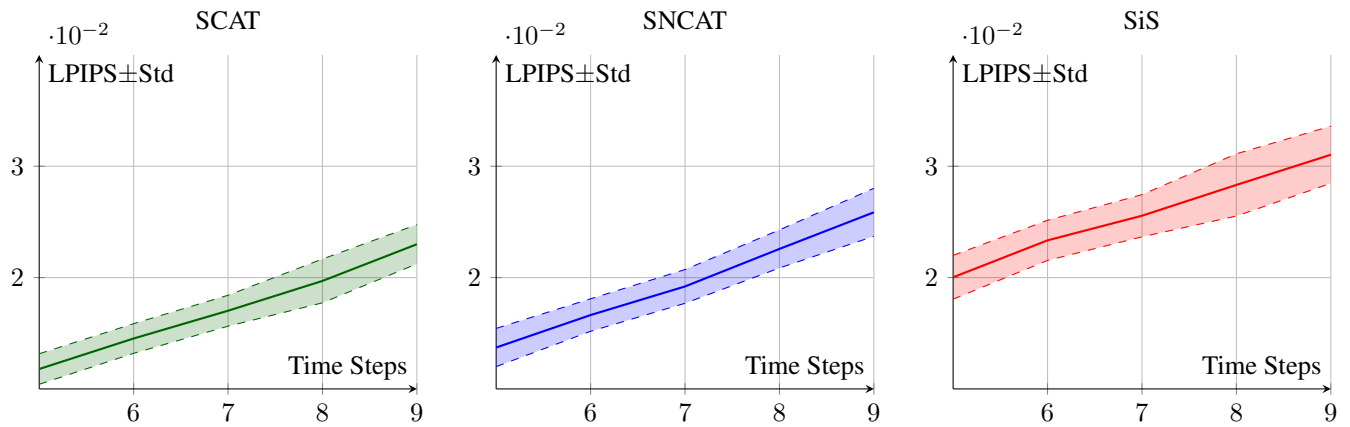


Figure 11: Mean and Std (Standard Deviation) of LPIPS metric on **Real-Traffic** dataset

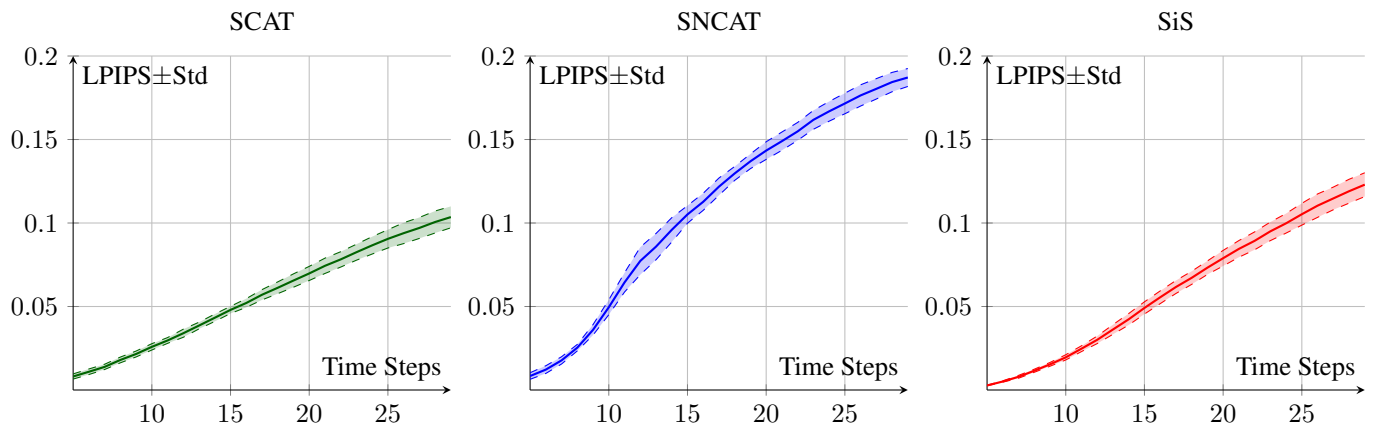


Figure 12: Mean and Std of LPIPS metric on **CLEVR-2** dataset

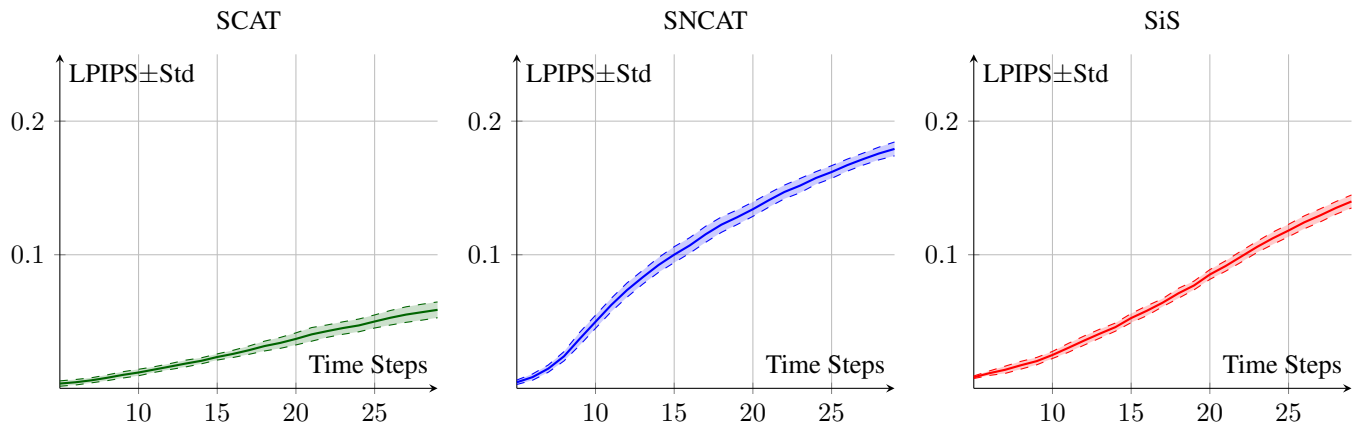


Figure 13: Mean and Std of LPIPS metric on **CLEVR-3** dataset

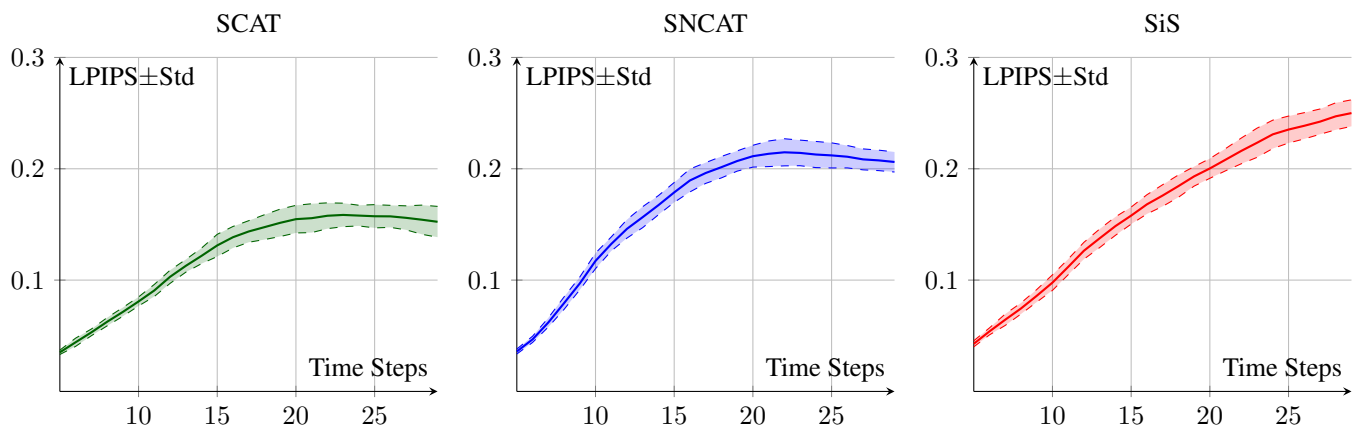


Figure 14: Mean and Std of LPIPS metric on **Kubric-Real** dataset

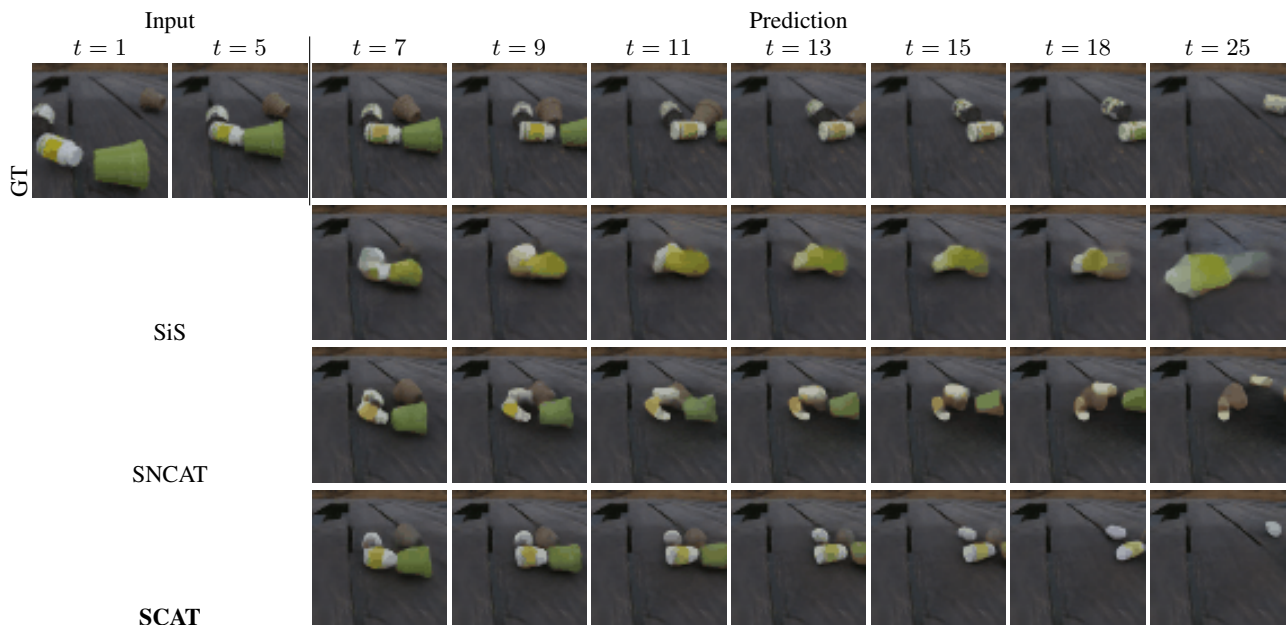


Figure 15: **Kubric-Real** Example 1

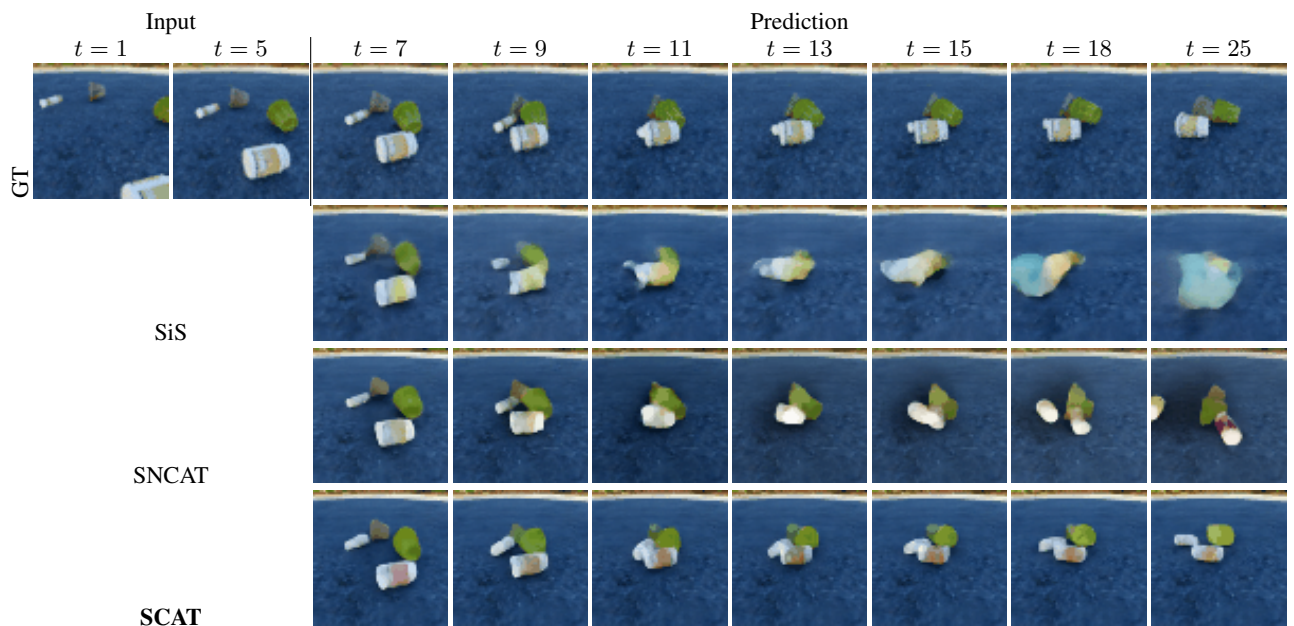


Figure 16: **Kubric-Real** Example 2

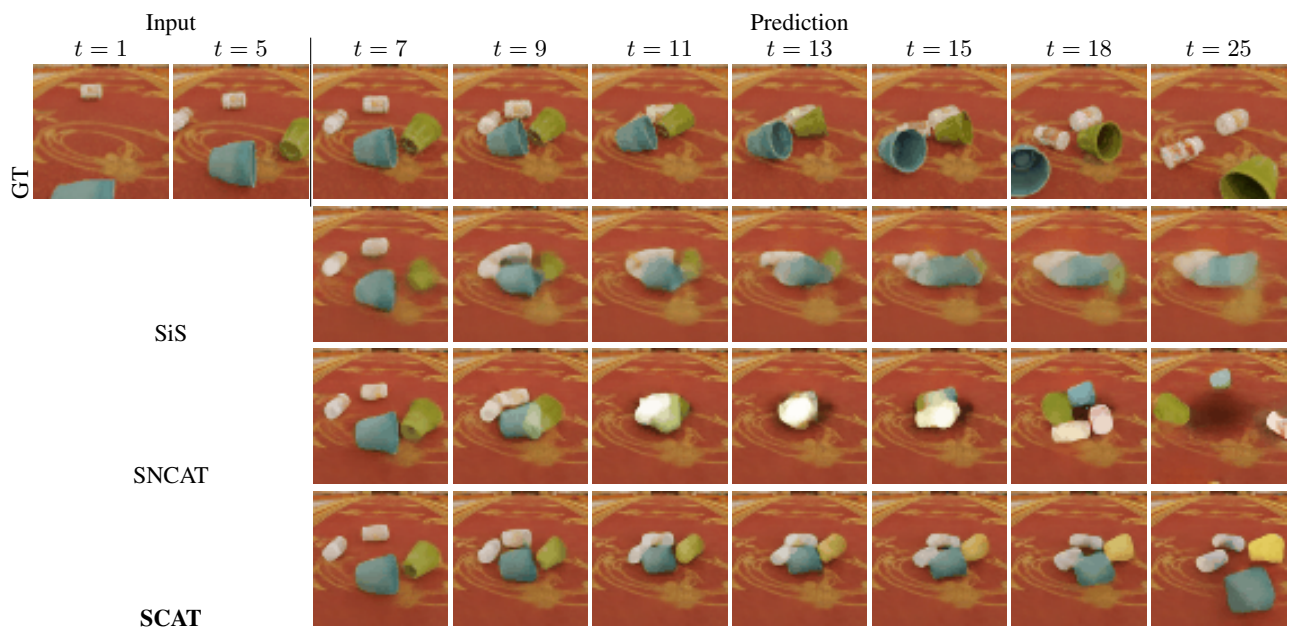


Figure 17: **Kubric-Real** Example 3

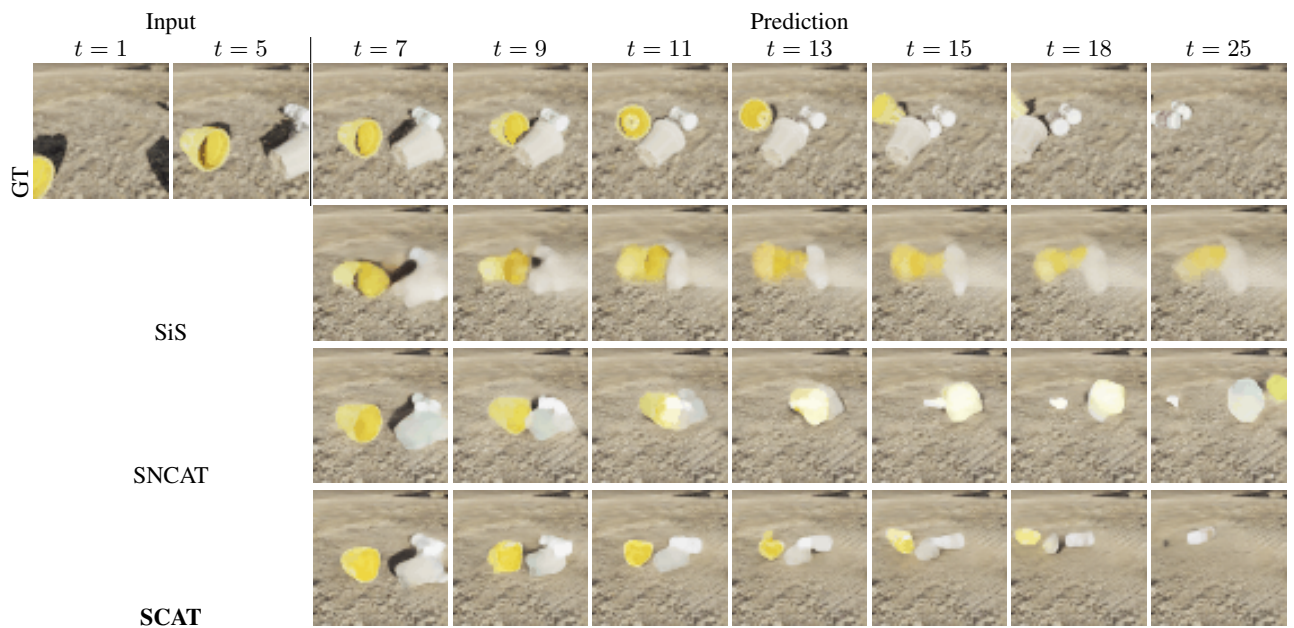


Figure 18: **Kubric-Real** Example 4

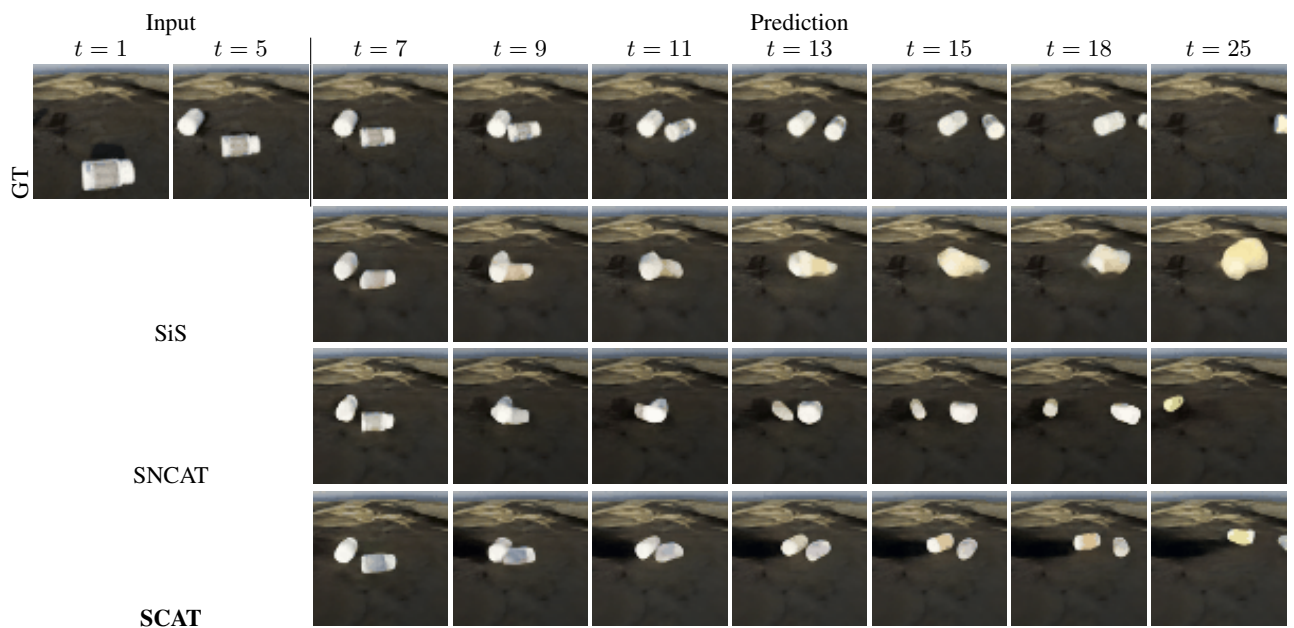


Figure 19: **Kubric-Real** Example 5

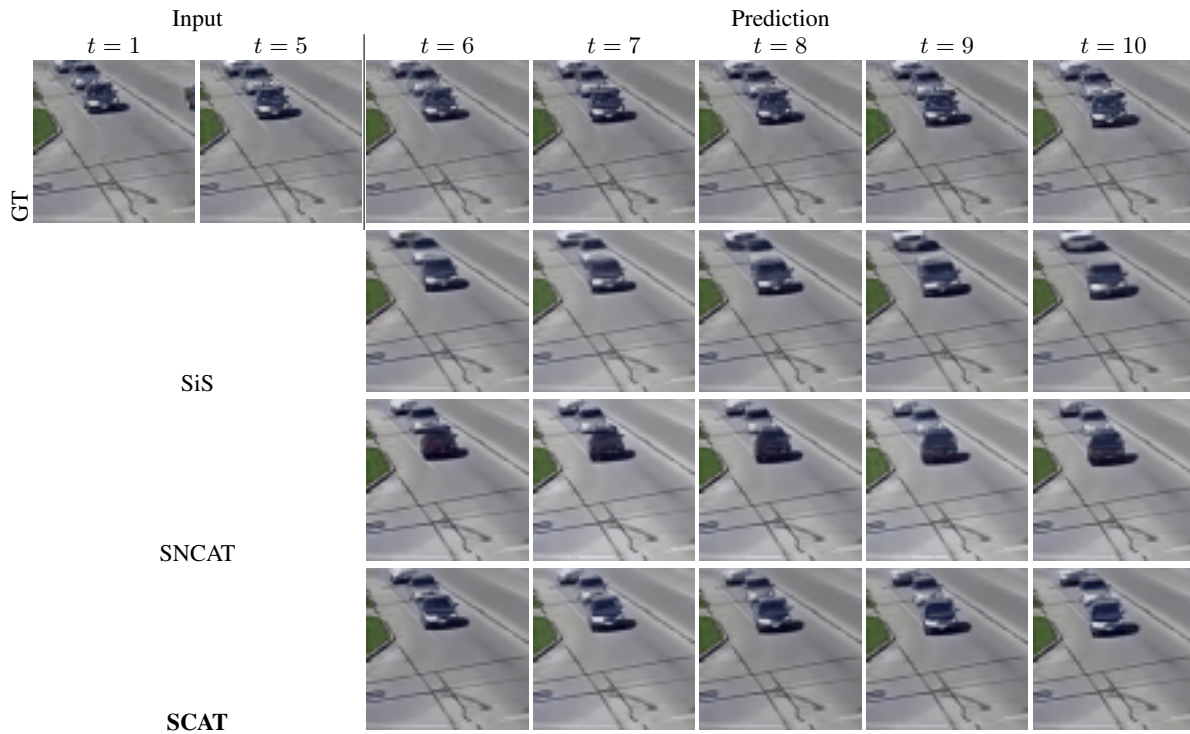


Figure 20: **Real-Traffic** Example 1

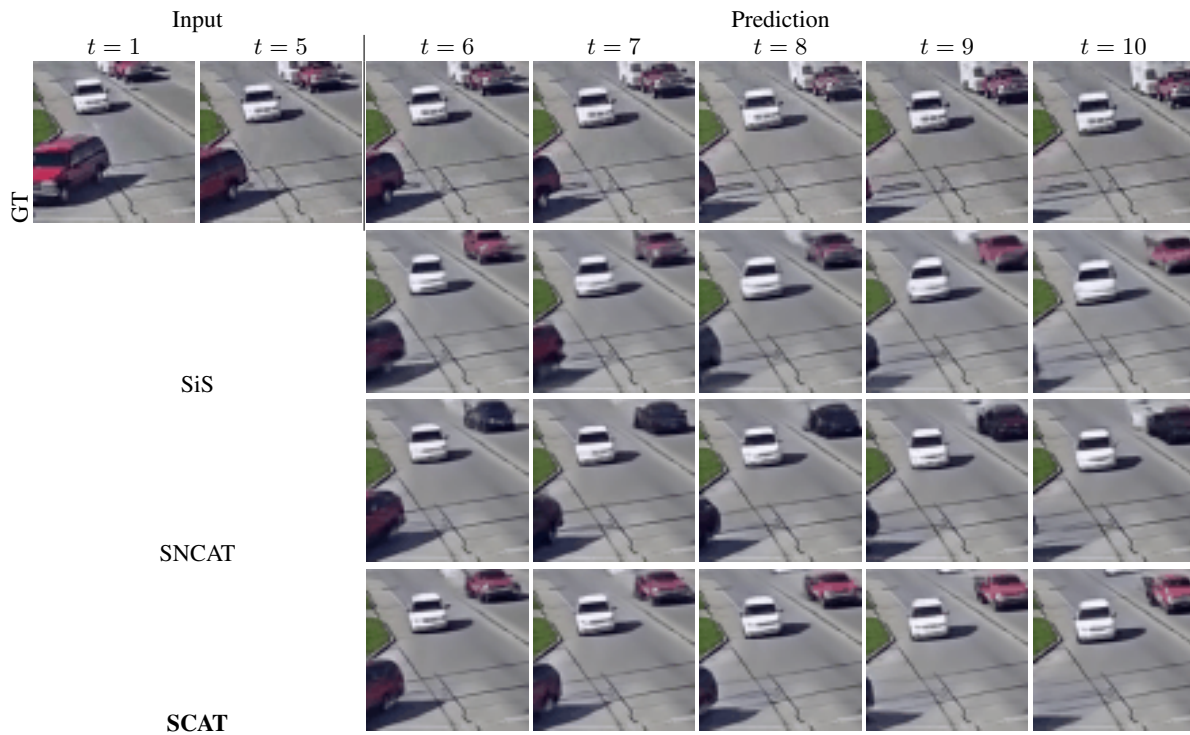


Figure 21: **Real-Traffic** Example 2

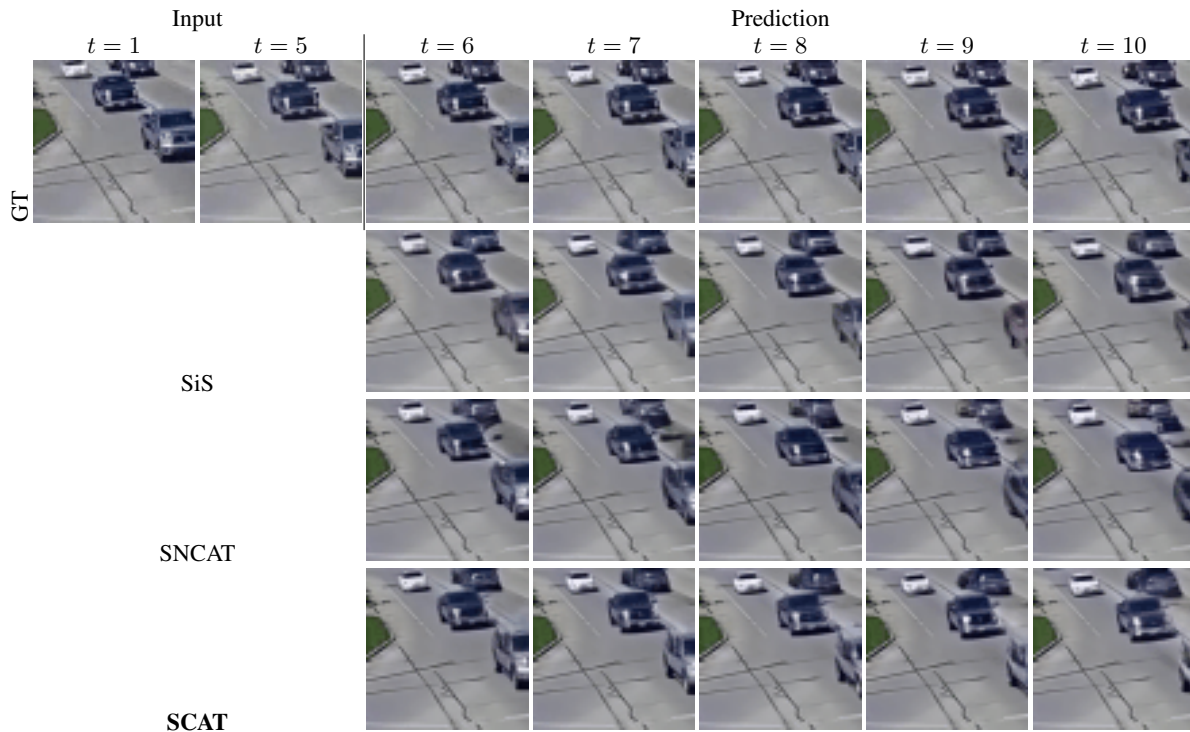


Figure 22: **Real-Traffic** Example 3

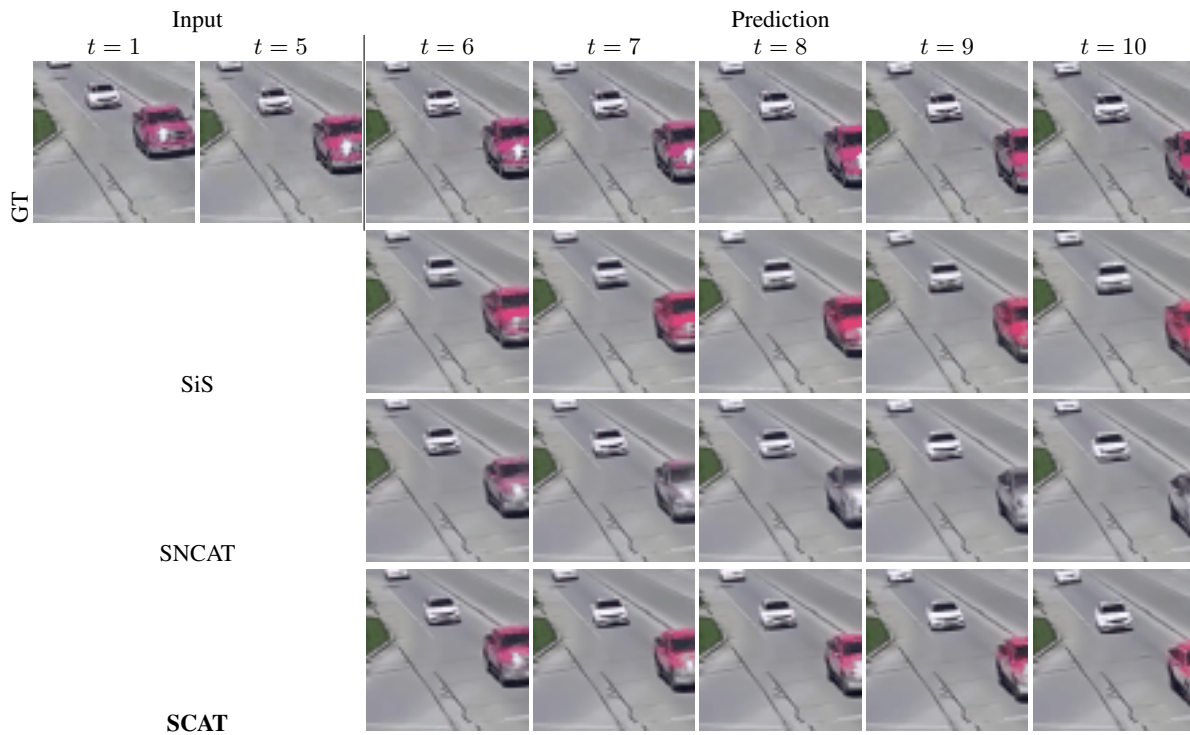


Figure 23: **Real-Traffic** Example 4

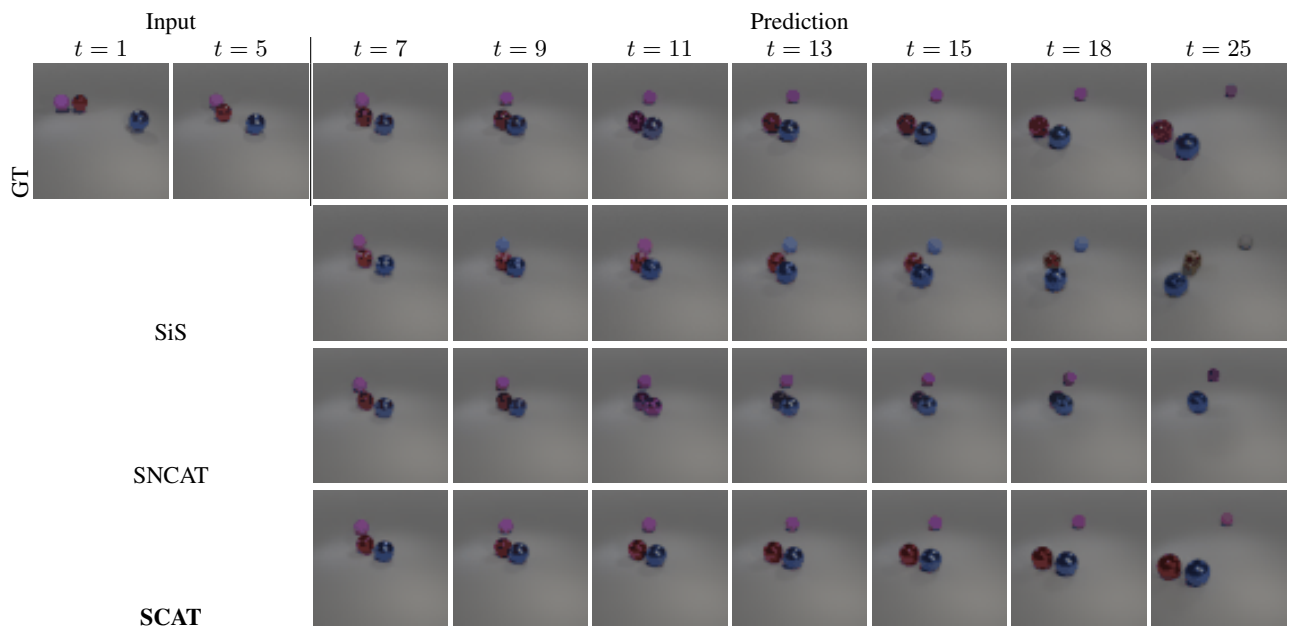


Figure 24: CLEVR-3 Example 1

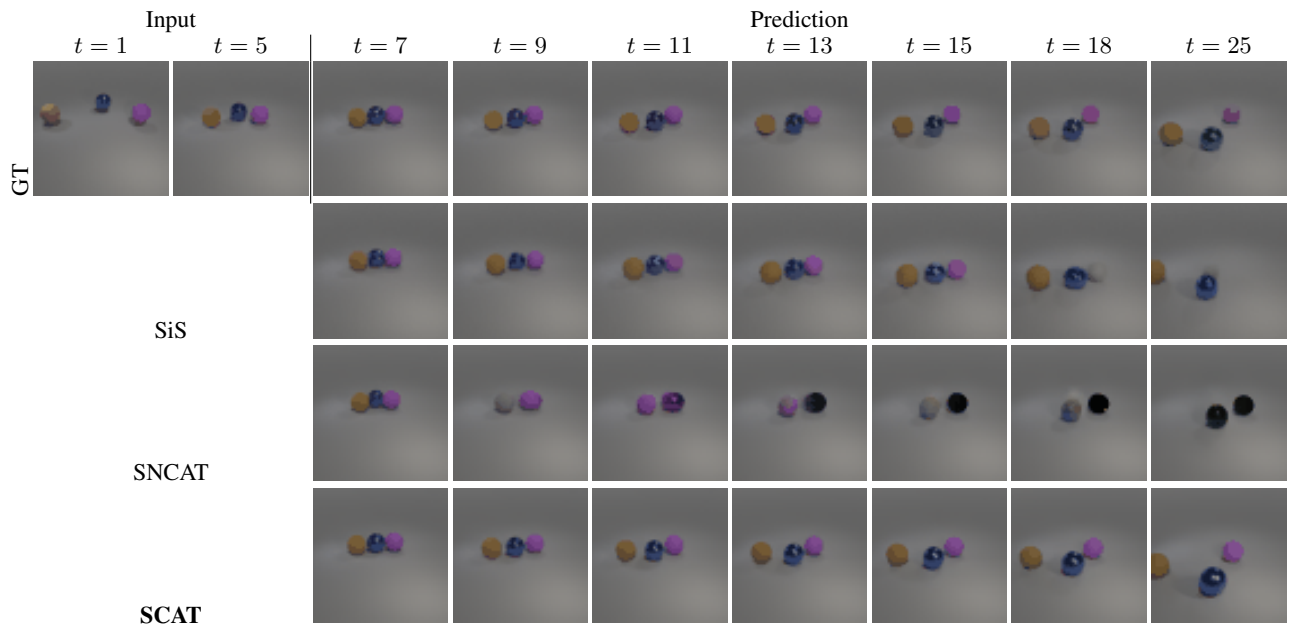


Figure 25: CLEVR-3 Example 2

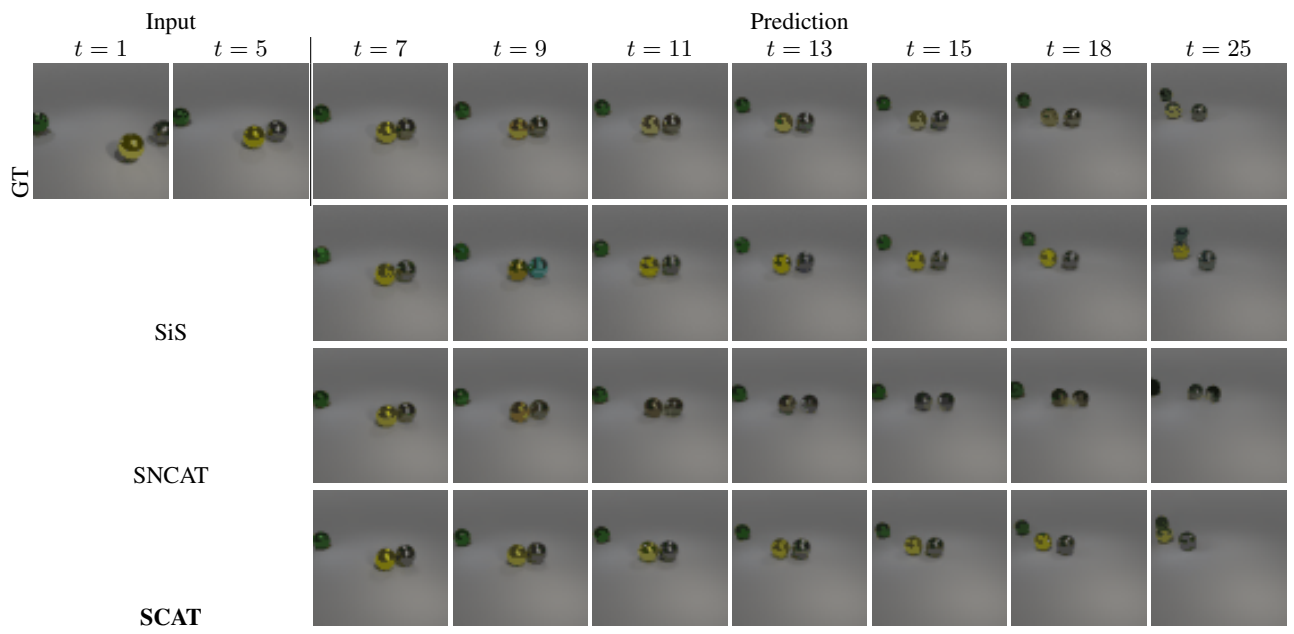


Figure 26: CLEVR-3 Example 3

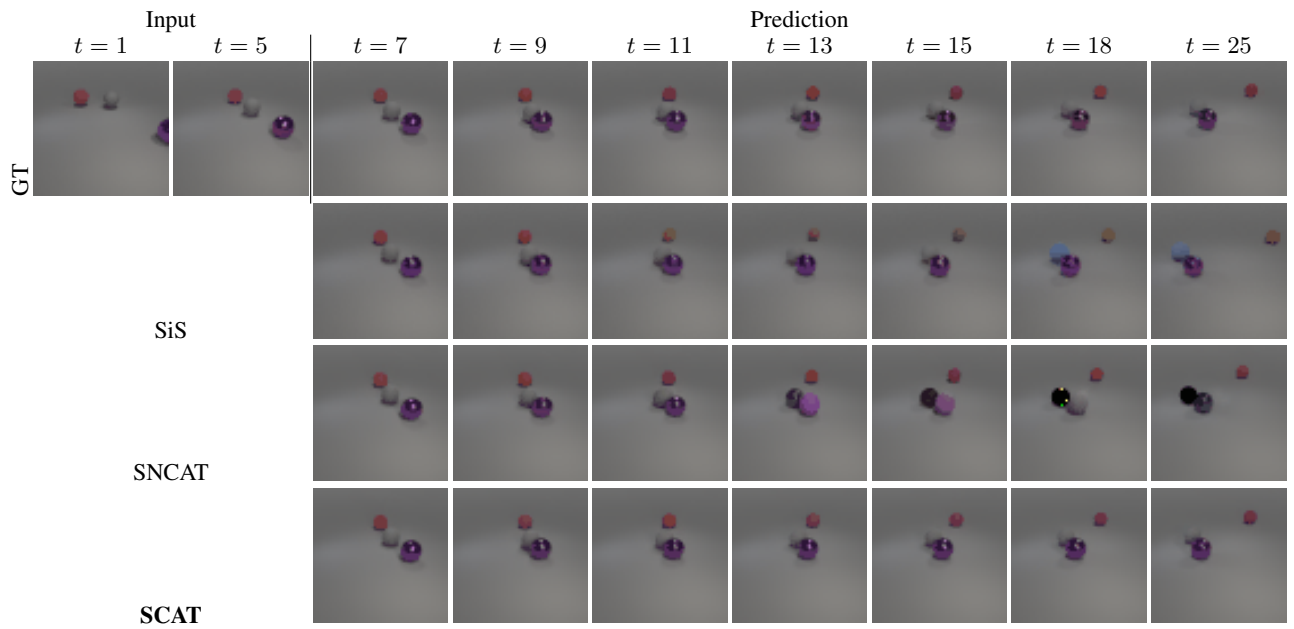


Figure 27: CLEVR-3 Example 4

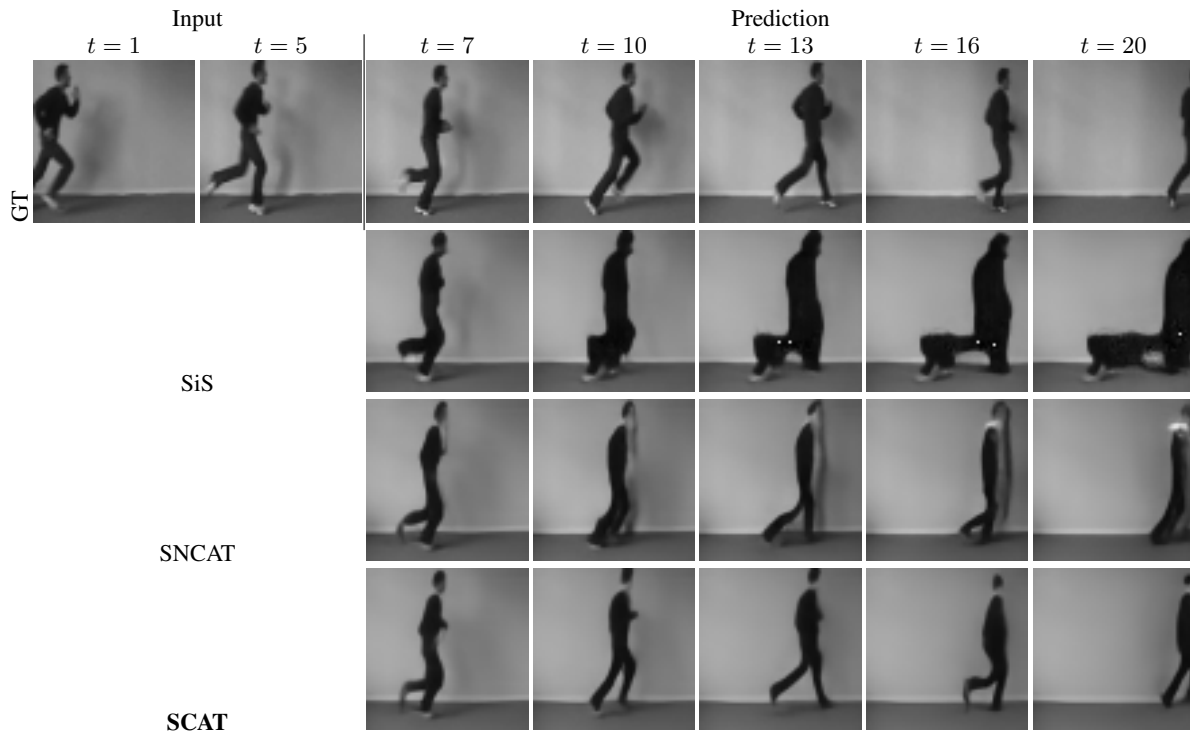


Figure 28: **KTH** Example 1

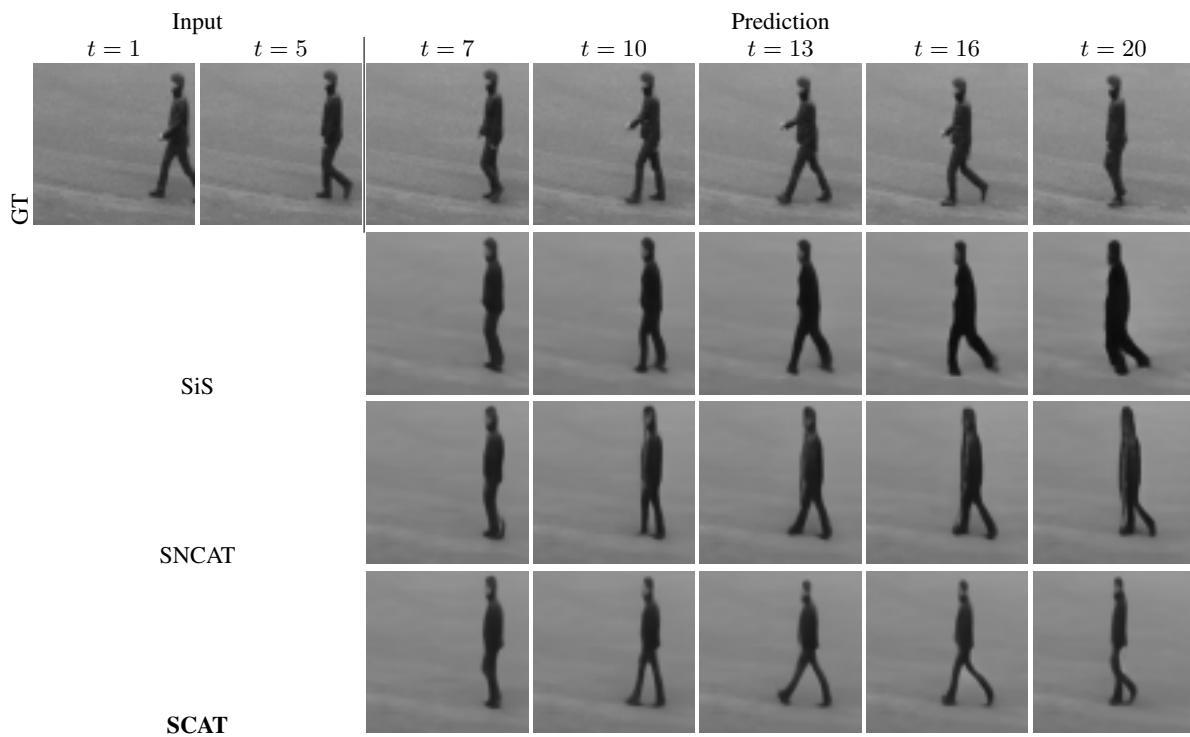


Figure 29: **KTH** Example 2

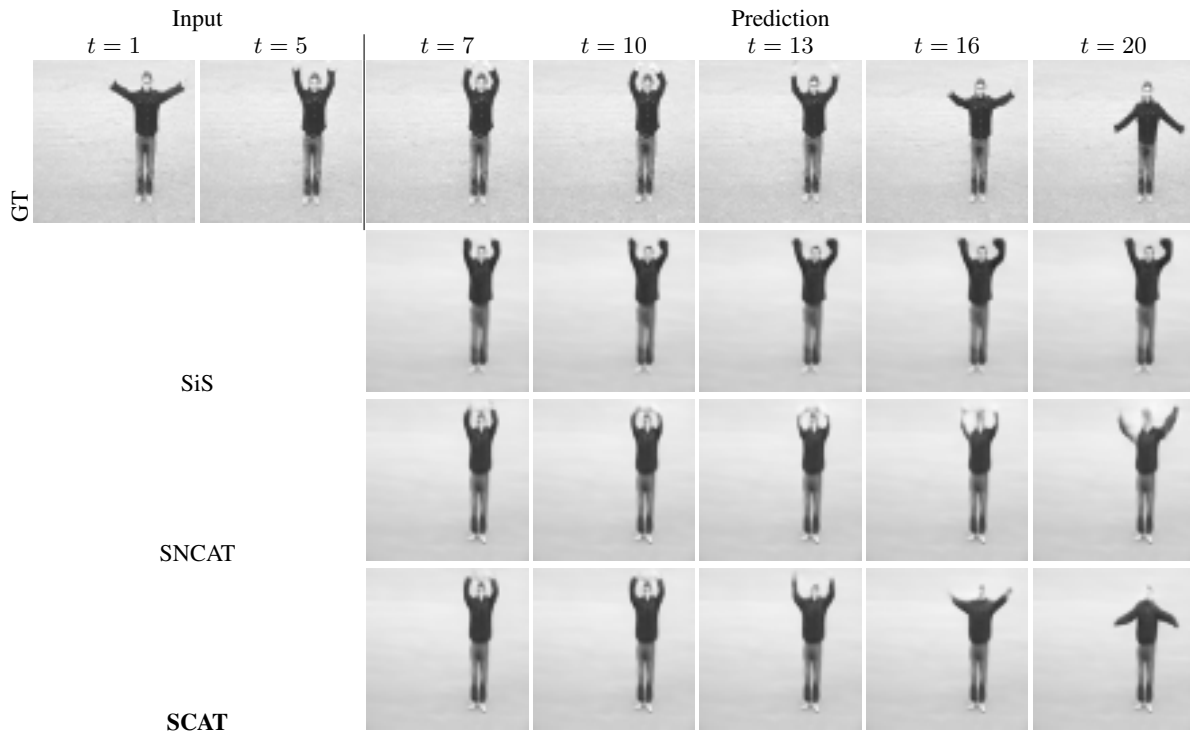


Figure 30: **KTH** Example 3

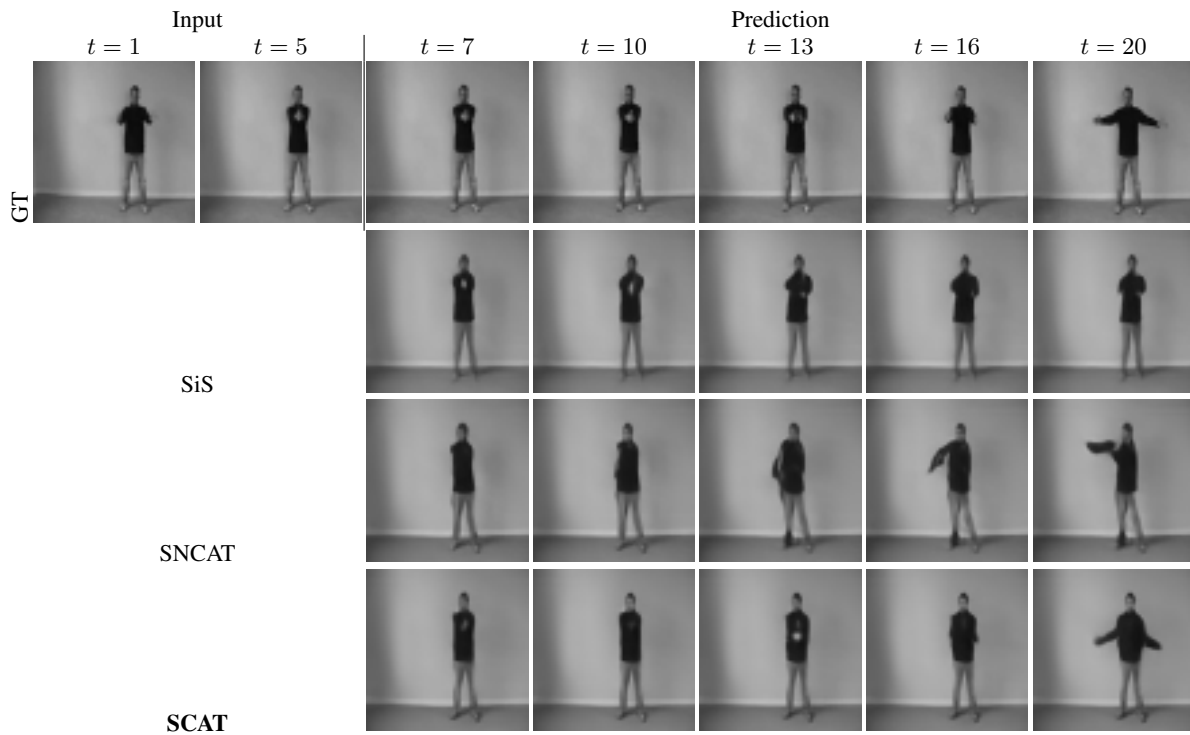


Figure 31: **KTH** Example 4

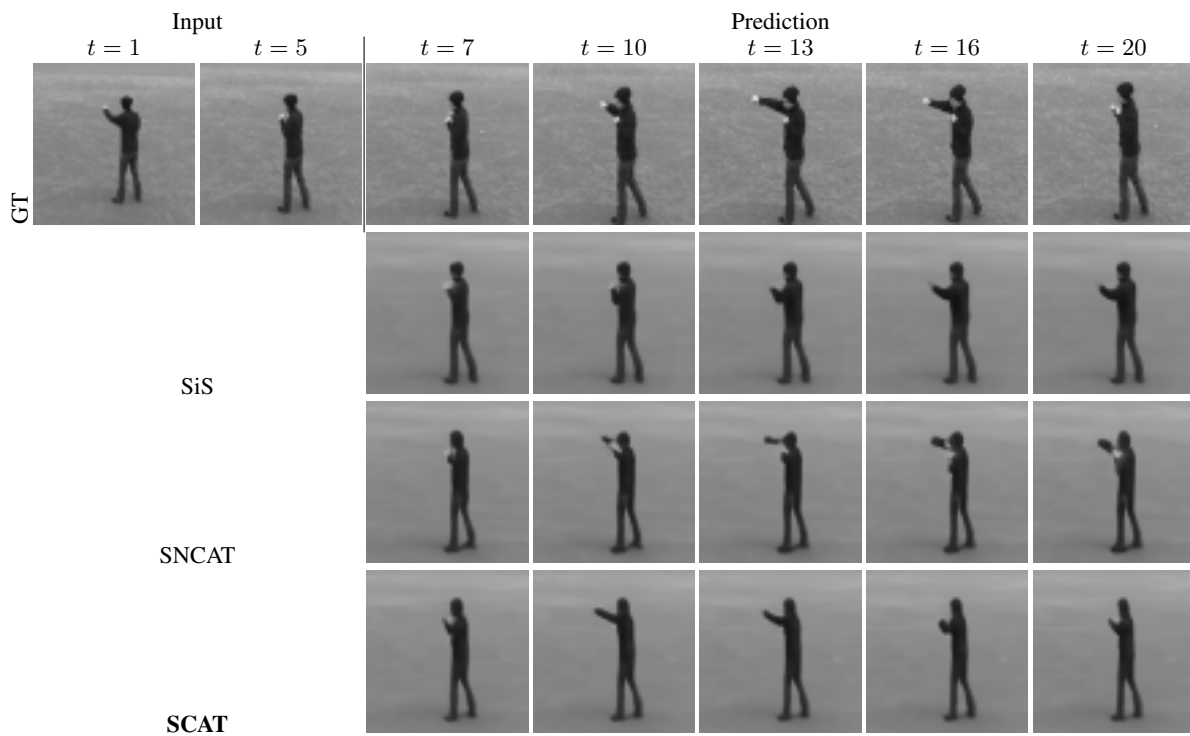


Figure 32: KTH Example 5